Ultrasonics Sonochemistry 95 (2023) 106371

Contents lists available at ScienceDirect

Ultrasonics Sonochemistry

journal homepage: www.elsevier.com/locate/ultson

Optimization of ultrasonic-assisted approach for synthesizing a highly stable biocompatible bismuth-coated iron oxide nanoparticles using a face-centered central composite design

Farhank Saber Braim [a,b,c,*], Nik Noor Ashikin Nik Ab Razak [a,*], Azlan Abdul Aziz [a,c], Mohammed Ali Dheyab [a,c,d], Layla Qasim Ismael [c]

[a] Nano-Optoelectronic Research and Technology Lab (NORLab), School of Physics, Universiti Sains Malaysia, 11800 Pulau Pinang, Malaysia
[b] Department of Biomedical Sciences, Cihan University-Erbil, Erbil, Iraq
[c] Nano-Biotechnology Research and Innovation (NanoBRI), Institute for Research in Molecular Medicine (INFORMM), Universiti Sains Malaysia, 11800 Pulau Pinang, Malaysia
[d] Department of Physics, College of Science, University of Anbar, 31001 Ramadi, Iraq

ARTICLE INFO

Keywords:
Fe_3O_4@Bi NPs
Sonochemical synthesis
Optimization
RSM
Zeta potential
Cytotoxicity

ABSTRACT

The incorporation of additional functional groups such as bismuth nanoparticles (Bi NPs) into magnetite nanoparticles (Fe_3O_4 NPs) is critical for their properties modification, stabilization, and multi-functionalization in biomedical applications. In this work, ultrasound has rapidly modified iron oxide (Fe_3O_4) NPs via incorporating their surface through coating with Bi NPs, creating unique Fe_3O_4@Bi composite NPs. The Fe_3O_4@Bi nanocomposites were synthesized and statistically optimized using an ultrasonic probe and response surface methodology (RSM). A face-centered central composite design (FCCD) investigated the effect of preparation settings on the stability, size, and size distribution of the nanocomposite. Based on the numerical desirability function, the optimized preparation parameters that influenced the responses were determined to be 40 ml, 5 ml, and 12 min for Bi concentration, sodium borohydride (SBH) concentration, and sonication time, respectively. It was found that the sonication time was the most influential factor in determining the responses. The predicted values for the zeta potential, hydrodynamic size, and polydispersity index (PDI) at the highest desirability solution (100%) were −45 mV, 122 nm, and 0.257, while their experimental values at the optimal preparation conditions were −47.1 mV, 125 nm, and 0.281, respectively. Dynamic light scattering (DLS) result shows that the ultrasound efficiently stabilized and functionalized Fe_3O_4NPs following modification to Fe_3O_4@Bi NPs, improved the zeta potential value from –33.5 to −47.1 mV, but increased the hydrodynamic size from 98 to 125 nm. Energy dispersive spectroscopy (EDX) validated the elemental compositions and Fourier transform infrared spectroscopy (FTIR) confirmed the presence of *Sumac* (*Rhus coriaria*) compounds in the composition of the nanocomposites. The stability and biocompatibility of Fe_3O_4@Bi NPs were improved by using the extract solution of the *Sumac* edible plant. Other physicochemical results revealed that Fe_3O_4NPs and Fe_3O_4@Bi NPs were crystalline, semi-spherical, and monodisperse with average particle sizes of 11.7 nm and 19.5 nm, while their saturation magnetization (*Ms*) values were found to be 132.33 emu/g and 92.192 emu/g, respectively. In *vitro* cytotoxicity of Fe_3O_4@Bi NPs on the HEK-293 cells was dose- and time-dependent. Based on our findings, the sonochemical approach efficiently produced (and RSM accurately optimized) an extremely stable, homogeneous, and biocompatible Fe_3O_4@Bi NPs with multifunctional potential for various biomedical applications.

1. Introduction

Magnetite nanoparticles (Fe_3O_4 NPs) have risen to prominence in many applications that facilitate the rapid advancement of nanoscale-based high-technology. Fe_3O_4 NPs have exhibited exceptional features, including ease of synthesis, small sizes, relative non-toxicity,

* Corresponding authors at: Nano-Optoelectronic Research and Technology Lab (NORLab), School of Physics, Universiti Sains Malaysia, 11800 Pulau Pinang, Malaysia (F.S. Braim).
E-mail addresses: farhank.braim@student.usm.my (F.S. Braim), nnashikin@usm.my (N.N.A.N.A. Razak).

https://doi.org/10.1016/j.ultsonch.2023.106371
Received 17 January 2023; Received in revised form 1 March 2023; Accepted 12 March 2023
Available online 15 March 2023

superparamagnetic crystal, and strong magnetic properties [1,2], and their potential as a promising candidate for a wide range of biomedical applications, such as targeted drug delivery, tumor detection and treatment, and magnetic resonance imaging (MRI) has been validated [3–5]. Despite extensive research on the exploration of Fe_3O_4 NPs, poor optical properties, and weak electrical conductivity hinders their widespread implementation [6]. Recent advances in Fe_3O_4 NPs research include not only the synthesis of homogeneous and stable core magnetic Fe_3O_4 NPs but also the formation of innovative nanostructures (functionalized surfaces, composites, core/shell, etc.) and the application of these nanomaterials in a variety of biomedical fields [7]. Composite NPs, particularly the core@shell structure that comprises distinct components, has recently been the subject of numerous investigations due to their unique physicochemical properties and multiple functionalities. The core@shell nanomaterials significantly improve intrinsic performance, overcome the restrictions of single-component properties, and exhibit a range of innovative features. Core@shell NPs typically composed of a core structure in the center and an exterior coated shell that varies in size, morphology, and organic/ inorganic interaction combinations. These NPs are capable of modifying the outer surface characteristics while retaining the properties of the inner core [8,9]. To stabilize and functionalize Fe_3O_4 NPs, researchers have investigated the possibility of coating their surface with organic molecules and polymers such as citric acid [10], malic acid [11], dextran [12], and chitosan [13]. However, it has been stated that the use of chemicals to coat the NPs could be costly and potentially hazardous to the environment [14]. Recent studies have indicated that plant-assisted synthesis can significantly reduce the toxicity of NPs while being economically advantageous and biologically safe. Our group has recently utilized extracts from the edible *Sumac* plant as a green stabilizer in the production of Fe_3O_4 NPs to reduce or eliminate the use of harmful compounds [15]. Besides, the application of Fe_3O_4 NPs can be expanded by incorporating new functional groups into their structure, such as gold (Au) [16], silver (Ag) [17], and bismuth (Bi) [18]. Owing to their exceptional properties, which include high chemical stability, low toxicity, cost-effectiveness, high X-ray attenuation coefficient, strong absorbance of near-infrared (NIR) light, and high photo-to-thermal conversion capability, Bi-based NPs have attracted considerable research interest for biomedical and *in vivo* applications [19]. Thus, Bi-incorporating Fe_3O_4 NPs are promising due to the combined advantages and properties of both components. However, the incorporation of Bi onto Fe_3O_4 NPs as a single nanostructure to form Fe_3O_4@Bi remains technically challenging due to their hurdle fabrication and handling issues for biomedical purposes.

Previous studies have significantly expanded the application of Fe_3O_4 NPs through the incorporation of Bi into Fe_3O_4 NPs structure, enabling the development of Fe_3O_4 NPs applications, such as double contrast agents for computed tomography (CT) scan and MRI, photothermal and magnetic hyperthermia therapies, and drug deliveries. Bismuth-iron oxide composite NPs have been synthesized by several methods, including aqueous co-precipitation [20–22], oxidative precipitation [23], conventional sol–gel [24], and bio-mineralization [25]. However, the majority of them were limited by lengthy reaction times and/or high reaction temperatures, complex procedures, and multiple reagents. The direct coating is an example of a technique that appears straightforward but is rather challenging due to the intricate steps of integrating two seemingly mismatched surfaces. In addition, the integration of Bi into the Fe_3O_4 core resulted in a hybrid NPs with extremely low saturation magnetization and non-superparamagnetic property [21]. Consequently, the incorporation of Bi into Fe_3O_4 must be technologically improved, particularly in minimizing hazardous reagents and controlling the particle size, magnetic characteristics, and composition of the NPs. Sonochemical (the application of high-intensity ultrasound) is a facile, rapid, non-conventional, and versatile approach that has been recently used to synthesize several types of NPs, which include iron oxide [26], bismuth [27], gold [28], and silver [29]. Additionally, the method has also been employed for coating and functionalizing organometallic molecules, organic polymers, and metallic on Fe_3O_4 NPs [30–32]. Sonochemical produces several unique conditions in a liquid, such as the acoustic cavitation process, which generates several physical and chemical effects, including microjets, shockwaves, highly reactive radicals as strong reducing and oxidizing agents, and heat known as localized hot spots [33]. The acoustic cavitation induced by ultrasound involves the generation, expansion (growth), and implosive collapse of bubbles, producing immense temperature, pressure, and high cooling rate of 5000 K, 2000 atm, and 10^{10} K/S, respectively. The main advantages of the sonication method for producing pure NPs with uniform sizes and shapes are a rapid reaction rate and controllable reaction conditions. [19,31].

It is critical to systematically design the experiment and optimize the fabrication process for the composite NPs to obtain the optimum result with a limited number of experiments. However, few reports highlighted the optimization of nanocomposites, and the protocol for optimizing the stability and hydrodynamic size of Bi/Fe_3O_4 composite NPs has not been established. Hence, Bi/Fe_3O_4 NPs need to be well dispersed and stabilized, and their hydrodynamic size must be optimized in an aqueous media, to prevent their adverse effects on biomedical and related applications. To achieve the maximum response from an experiment with minimum time and resources, methods must be optimized to find the best combination of various detectable experimental parameters that influence the results (quality of the product). Response surface methodology (RSM) has been extensively used to develop and optimize various NPs [6,34,35]. RSM is a powerful mathematical and multivariate statistical technique for analyzing experimental conditions in a theoretical design through the response function [30]. Compared to other sub-sets, central composite design (CCD) has more center points, and it is an accurate and crucial component of RSM that provides superior predictions within the design space. In particular, face-centered CCD is utilized to examine extreme conditions or values, leading to a better quadratic design [36].

Therefore, the present study aims to synthesize, functionalize, and statistically optimize Bi-coated Fe_3O_4 in a single core@shell probe via an ultrasonic irradiation approach. To the best of our knowledge, sonochemical synthesis and optimization of Fe_3O_4@Bi composite NPs have not been reported. In this study, we used a seeding growth-mediated approach, where Fe_3O_4 NPs were used as a template for the growth of BiNPs. For this purpose, we initially synthesized stable Fe_3O_4 NPs through the co-precipitation method. Subsequently, we modified their surface via coating with BiNPs by the sonochemical method using a Vibra-Cell ultrasonic probe with a tip size horn, frequency, amplitude, and power of 1.3 cm, 20 kHz, 40%, and 750 Watts, respectively. Due to its strong affinity for hydroxide ions, Bi^{3+} eventually promotes precipitation in a colloidal suspension, resulting in the agglomeration and rapid oxidation of the NPs. To address this issue, most previous studies utilized organic polymers in the preparation of Bi-containing NPs [19,37,38], which are costly synthetic reagents. However, similar to our recently reported [15], this study has used an efficient, low-cost, and bio-safe of *Sumac* extract as a green stabilizer for the synthesis of Fe_3O_4@Bi NPs. Nonetheless, DLS has been analyzed initially and the influence of ultrasonic irradiation time and power was specifically investigated on stability and size. We were able to identify the variables (such as bismuth (Bi) concentration, sodium borohydride (SBH) concentration, and sonication time) and their interactions that affected the Zeta potential (ζ) value, hydrodynamic size, and polydispersity index (PDI) of the NPs using the statistical experimental design controlled by face-centered central composite design (FCCD). Eventually, the responses were optimized by RSM and the physicochemical properties of the optimized Fe_3O_4@Bi NPs were characterized using X-ray diffraction (XRD), RAMAN, FTIR, Field Emission Scanning Electron Microscopy (FESEM), Transmission Electron Microscope (TEM), EDX, UV–visible, and Vibrating Sample Magnetometer (VSM). Furthermore, the toxicity of the NPs was evaluated by the MTT assay in normal HEK-293 cells. The results confirm that ultrasound was efficiently synthesized and

incorporated BiNPs with Fe_3O_4 NPs in a novel nanostructure of Fe_3O_4@Bi. In addition, the NPs are highly stable, monodisperse, and biocompatible, with the potential for a wide range of biomedical applications.

2. Materials and methods

2.1. Reagents

Ferric chloride ($FeCl_3{\cdot}6H_2O$, $\geq$ 98%), ferrous chloride ($FeCl_2{\cdot}4H_2O$, 98%), glycine ($C_2H_5NO_2$), and bismuth nitrate pentahydrate ($Bi(NO_3)_3{\cdot}5H_2O$, 98%) were purchased from Sigma-Aldrich. Concentrated ammonium hydroxide (NH_4OH, 28–30%) and sodium borohydride (SBH, $NaBH_4$) were obtained from Merck. Mature and dry *Sumac* (*Rhus coriaria*) seeds were collected on a farm from the Akre area in the Kurdistan region, Iraq. The seeds were then ground into powder using a mortar and pestle.

2.2. Preparation of Sumac extract

To prepare the extract solution from the *Sumac*, a total of (2 g) of *Sumac* powder was mixed with 100 ml of (60% ethanol, and 40% autoclaved deionized (DI) water) in a 250 ml of Erlenmeyer flask and incubated at room temperature for 48 h. The mixture was stirred for 5 min at 500 rpm after each 12 h. Ultimately, the ethanolic extract solution was filtered using gauze and filter paper. Followed by, the ethanol was completely evaporated from the extract solution. The remaining solution was then added by 60 ml autoclaved DI water, filtered by a Millipore filter (0.22 μm), and stored at 4 °C for next use.

2.3. Synthesis of Fe_3O_4 NPs

Recently, our group successfully reported the synthesis of Fe_3O_4 NPs through a green-assisted co-precipitation technique [15]. Briefly, 1.11 g of ferric chloride and 0.5 g of ferrous chloride were separately dissolved in 35 ml of DI water, mixed in a three-neck round-bottom flask, and mechanically stirred under the flow of N_2 gas at 680 rpm. Afterward, 10 ml of NH_4OH was dropwise added to the iron mixture and heated up to 70 ± 3 °C for 10 min. To stabilize and prevent the NPs from agglomeration, and functionalize their surface, 5 ml of *Sumac* extract solution was added to the reaction mixture while continuously stirring under the same stirring rate and temperature for 15 min. A permanent magnet then collected the colloidal suspension of Fe_3O_4 NPs, thoroughly washed three times with DI water to eliminate any unreactive contaminants, and re-dispersed in DI water.

2.4. Synthesis of Fe_3O_4@Bi NPs

Synthesis of Bi-coated Fe_3O_4 NPs was based on the seeding growth mediated approach, in which Fe_3O_4 NPs were initially prepared as core seeds and then used as a template to grow Bi NPs as a shell via the reduction of $Bi(NO_3)_3{\cdot}5H_2O$ by $NaBH_4$ and the ultrasonic irradiation. Sonochemical was carried out using a Vibra-Cell probe with a tip-size horn, frequency, and power of 1.3 cm, 20 kHz, and 750 W, respectively. $Bi(NO_3)_3{\cdot}5H_2O$ salt was dissolved in glycine solution (0.25 M) to prepare Bi solution (1 mM). The colloidal suspension of Fe_3O_4 NPs (3 ml, 1.25 mg Fe/ ml) was mixed with Bi solution at different concentrations (Table 1), and the mixture was sonicated for 1 min. Afterward, 3 ml of the aqueous *Sumac* extract was added, the pH was adjusted to 9, and the mixture was sonicated for another 3 min. The resultant mixture was subsequently subjected to varying concentrations of SBH ($NaBH_4$, 0.05 M) and varied sonication periods (8, 10, and 12 min) at corresponding powers of (30, 35, and 40 W), as established by the software for the design of experiments (DOE) and displayed in Table 1. Finally, the resultant Fe_3O_4@Bi NPs were re-collected, isolated, and thoroughly washed with DI water to remove non-reactive impurities and re-dispersed in DI water.

Table 1
Independent variables and their corresponding levels for FCCD of Fe_3O_4@Bi NPs.

Symbols	Factors	Units	Coded Levels		
			Low (-1)	Medium (0)	High (+1)
X_1	Bi concentration	ml	20	30	40
X_2	SBH concentration	ml	5	10	15
X_3	Sonication time	min	8	10	12

2.5. Experimental design using RSM

The design of the experiment is an extremely useful method for modeling and analyzing the impact of process variables on response variables. To achieve the most precise findings, an experiment should be designed scientifically. Response surface methodology (RSM) is an advanced and widely utilized experimental design for optimization. It enables the assessment of the effects of several factors (parameters that affect the process) and their interactions on one or more response variables. An experimental fractional factorial design known as the central composite design (CCD) is frequently used in RSM to construct a second-order quadratic model for the response variables. In CCD, there are three distinct points: factorial points, central points, and axial points. Factorial points are the vertices of an n-dimensional cube that originate from a complete or fractional factorial design in which the factor levels are encoded as −1 and 1. The central point is the point located at the center of the design area. Axial points are symmetrically located on the axes of the coordinate system concerning the central point at a distance (α) from the design center [39,40]. In this study, as an optimization tool of RSM, CCD was applied to explore the impact of formulation variables on the properties of Fe_3O_4@Bi NPs produced by the sonochemical method. Based on our test (preliminary) data, face-centered central composite design (FCCD) has been selected as a viable fitting model to establish the optimal experimental settings and process. It is a type of CCD from which the axial points are located at the face centers of the design factorial spaces, each factor has three levels, and alpha (α) is equal to 1. This design typically models the response with a second-order polynomial equation, allowing estimation of the primary, quadratic, and interaction impacts of the investigated factors (independent variables) on the properties. In FCCD, the formula for the number of experimental samples can be represented as ($2^{k} + 2k + n$), where k denotes the number of factors and n denotes the number of center points (are the replicates in the center) [41]. Thus, our study was designed based on FCCD, containing seventeen (17) experimental runs, which consisted of eight factorial points, three center points to calculate the experimental errors and data reproducibility [35], and six stars (axial) points at three experimental levels (k = 3, n = 3). This experimental matrix determines the effect of three factors (independent variables), which are Bi concentration (X_1), SBH concentration (X_2), and sonication time (X_3) on three responses (dependent variables); zeta potential value (Y_1), hydrodynamic particle size (Y_2), and polydispersity index (PDI) (Y_3). The data were evaluated using a response surface regression technique, and a polynomial model was selected based on the significant terms ($p < 0.05$) using Design-Expert 13 software (Stat-Ease, Inc., Minneapolis, MN, USA). The low, medium and high levels of independent variables are exhibited in Table 1.

The predicted responses were investigated and indicated by using a second-order polynomial equation as a function of independent variables, as shown in Eq1:

$$Y = \beta_0 + \sum_{i=1}^{k} \beta_i X_i + \sum_{i=1}^{k} \beta_{ii} X_i^2 + \sum_{i=1}^{k} \sum_{j=1}^{k} \beta_{ij} X_i X_j \quad (1)$$

where Y denotes the predicted responses (zeta potential, hydrodynamic

size, and PDI), β_0 is the model constant, X_i and X_j are the coded independent variables, β_i, β_{ii}, and β_{ij} are linear, quadratic, and interactive (cross-product) coefficients, respectively.

2.6. Statistical analysis

A number of statistical characteristics, including lack-of-fit, predicted and adjusted multiple correlation coefficients, and coefficient of variation of various polynomial models were evaluated to determine the best-fitting model. The significance of the differences between the factors was assessed to determine the adequacy of the developed models using the analysis of variance (ANOVA) with a confidence level of 95%. The model contained all significant factor effects, a ($p < 0.05$) was considered significant, and a satisfactory fit required a regression coefficient (R^2) of at least 0.8 [36]. Three-dimensional (3D) plots of the response surface were generated by the Design Expert software (version 13) to depict the influence of the independent variables on the responses.

2.7. Characterization

The structure and composition of the NPs were evaluated by X-ray diffraction (XRD, PANanalytical X'pert PRO MRD PW 3040 with Cu-Kα radiation (λ = 1.54060 A°)). The morphology, size, and size distribution of the produced Fe_3O_4 NPs and Fe_3O_4@Bi NPs were characterized and determined using Field Emission Scanning Electron Microscopy (FE-SEM, Hitachi Ultrahigh Resolution SEM Regulus8230), Transmission Electron Microscope (TEM, Zeiss Libra 120 at 100 kV), and ImageJ 1.53e software. The absorption properties of the NPs were investigated using a UV–vis-NIR spectrophotometer (UV-3600i, Shimadzu). Energy dispersive X-ray (EDX, analyzer Oxford Instruments X-Max) was deployed to identify elements present in the synthesized NPs. Raman spectroscopy (Renishaw in Via spectrometer) was used to analyze the Bi and Fe_3O_4 structure in the composition of Fe_3O_4@Bi NPs. Fourier transform infrared spectroscopy (FTIR, Thermo Fisher Scientific Nicolet iS1O FTIR spectroscopy) has been used to identify the functional groups adsorbed on the surface of the NPs. Dynamic Light Scattering (DLS, Malvern Instruments, ZETASIZER Nanoseries Model ZEN 3600) was used to measure the Zeta potential value (stability), hydrodynamic particle size, and PDI of the NPs. The magnetic properties of the NPs were evaluated using Vibrating Sample Magnetometer (VSM, LAKESHORE MODEL 7404).

2.8. Cytotoxicity

To assess the in *vitro* cytotoxicity of Fe_3O_4@Bi NPs, HEK-293 cells were used via a standard MTT assay. HEK-293 cells were grown in DMEM containing (FBS, 10%) and (penicillin/streptomycin, 1%) at 37 °C in 5% CO_2 and 95% humidity. After 24 h, the cells were trypsinized, seeded in 96-well plates at a density of 1×10^4 per well in 100 µl of complete DMEM, and incubated at 37 °C for 24 h. The cells were then treated with Fe_3O_4@Bi NPs at different concentrations of (0, 50, 100, 200, 300, and 400 µg/ ml) and incubated for 24, 48, and 72 h. After each time point, 30 µl MTT (25 mg/ 10 ml PBS) was added to each well and the plates were incubated for 4 h at 37 °C. Then the medium was completely removed, the DMSO (100 µl/ well) was replaced, and the plates were incubated for 5 min to dissolve the crystals. Lastly, the absorbance of the samples was measured at 570 nm wavelength using the micro-plate reader (ELx800, BioTek Instruments, USA).

3. Results and discussion

Irradiation of liquids with ultrasonic waves leads to the production of acoustic cavitation (bubble formation, growth, and collapse). The collapsing bubbles convert potential energy into effective temperature and pressure of about 5000 K and 1000 atm, as well as creating hot spots. Alongside these localized hot spots, acoustic cavitation produces shockwaves or microjets. The dynamics of shockwaves and microjets are liquid environment-dependent. In a homogenous liquid, acoustic cavitation and shock waves are generated when the substance in the medium is smaller than the collapsing bubbles (~150 nm). Therefore, Fe_3O_4@Bi nanocomposites have been synthesized under the influence of the acoustic cavitation process with the creation of shock waves. The shockwaves are capable of generating enormous pressure and moving at a high speed, thereby inducing turbulence flow and rapid mechanical stirring in the liquid material [32]. In this study, this technique has been applied for driving chemical reactions, improving the reaction and collision rates, and rapidly coating the Bi shell onto the Fe_3O_4 core under extreme conditions. The formation procedure of Fe_3O_4@Bi NPs involved two stages. In stage 1, the magnetite NPs were synthesized via the green-assisted co-precipitation method using *Sumac* extracts as a green stabilizer and capping agent. In stage 2, as shown in Fig. 1, the as-synthesized Fe_3O_4 NPs were used as a template to grow the Bi NPs layer on their surface to form the Fe_3O_4@Bi composite NPs in a single core@shell structure using the sonochemical method. Specifically, the Fe_3O_4 seed NPs ultrasonically dispersed in bismuth nitrate solution, the Bi NPs shell formed on the Fe_3O_4 NPs through the $NaBH_4$ reduction of Bi ions, followed by *Sumac* extract addition to stabilize and functionalize their surfaces with various biomolecule functional groups from the extract solution. These biomolecules consisted of tannins, flavonoids, and many other phenolic compounds that are abundant in *Sumac* [15]. Thus, the *Sumac* extract solution stabilized and functionalized the synthesized NPs, and enhanced the attachment of Bi NPs on the surface of Fe_3O_4 NPs.

3.1. Fitting the model

In this work, the experiment was designed using RSM with FCCD. Based on the experimental designs, the effect of three operating factors on the synthesis and functionalization of the NPs was investigated. Design Expert was utilized for statistical regression analysis of experimentally collected values, drawing response surfaces, and plotting at the optimal condition. The details of the experimental design matrix and the responses are shown in Table 2. The optimum independent variables (Bi concentration, SBH concentration, and sonication time) for Fe_3O_4@Bi NPs formulation were chosen based on obtaining smaller hydrodynamic particle size, PDI, and higher zeta potential value (stability) under the DOE conditions. The selected models proposed by the software were quadratic, linear, and linear models for the zeta potential, hydrodynamic size, and PDI of the NPs, respectively. To predict the response values, coefficients of the polynomial equation were calculated from the experimental data. Regression equations were obtained from the RSM for each response variable, and each model's resulting coded equation as a function of actual factors can be established in Eqs. (2) - (4):

$$Y_1(Zetapotential) = -46.52 - 4.61X_1 - 1.32X_2 - 4.12X_3 - 1.48X_1X_2 - 2.01X_1X_3 - 1.99X_2X_3 + 1.78X_1^2 + 2.13X_2^2 + 3.27X_3^2 \quad (2)$$

$$Y_2(Hydrodynamicalsize) = +153.03 + 18.65X_1 + 13.95X_2 - 35.55X_3 \quad (3)$$

$$Y_3(Polydispersityindex) = +0.2925 + 0.0236X_1 + 0.0088X_2 - 0.0501X_3 \quad (4)$$

Statistical analysis of the design starts with (ANOVA) for the models and independent variables (Tables 3a and b). The most effective parameters were identified based on the *p*-value and *F*-value. The influence of a highly significant term on a response is indicated by a greater *F*-value and smaller *p*-value [42]. The (ANOVA) results indicated that a linear quadratic polynomial could adequately represent the experimental data, and linear models with R^2 values of 0.9807, 0.8552, and 0.9209 for the zeta potential, hydrodynamic size, and PDI, respectively (Table 3b). R^2 is the accuracy of the models and measures how well a

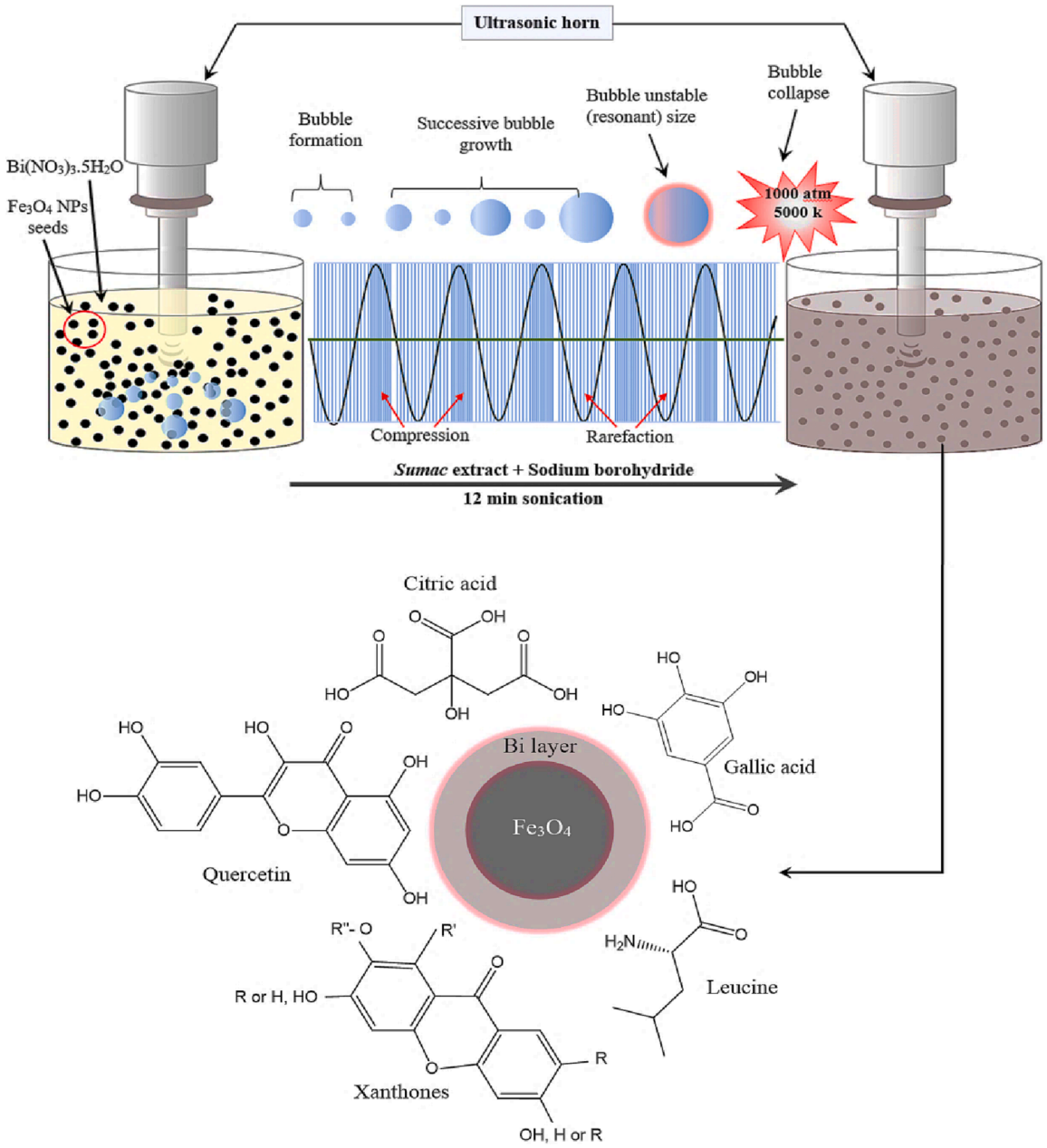

Fig. 1. Schematic representation of the synthesis and functionalization of Fe_3O_4@Bi composite NPs.

model fits the data, and a number closer to one implies better model fitting [42]. The extremely low *p*-value (<0.0001) indicates the highly significant of the model and the factors for the data prediction relate to response within a 95% confidence interval. Hence, it can be clearly observed in (Table 3a) that the linear terms, including X_1 and X_3 in all three models, their interactions, and quadratic of $(X_3)^2$ in the quadratic model significantly affected the responses. However, X_3 (sonication time) showed the most significant effect (*p*-value < 0.0001). Table 3a also shows that the liner term X_2 (SBH concentration) had the lowest influence on the responses Y_1 and Y_2 in the first and second but had no significant effect on Y_3 in the third suggested models. Relative to pure error, the lack of fit in each model was not statistically significant ($p \geq 0.05$), demonstrating the statistical accuracy of our models.

Fig. 2(a-f) shows the normal plot of residuals and predicted versus actual values for the responses. The diagnostics of the statistical models are depicted in Fig. 2(a, c, and e) as the majority of the residuals fell on a straight line, provided a roughly linear set of data points, and distributed errors regularly, indicating a higher significance. The correlation between expected and actual responses is displayed in Fig. 2(b, d, and f), which shows no significant difference in the values; thus, the values adequately conform to the range of the functional variables.

3.2. *Effect of operating parameters on response variables*

Fe_3O_4@Bi NPs were successfully synthesized using different independent variable levels (Fig. 2) through the sonochemical method. The influence of independent variables on the zeta potential, hydrodynamic size, and polydispersive index of the NPs are provided in Table 2. Regression coefficients for independent variables in each model are summarized in Table 3.

The last essential step consisted of determining the variables' conditions that maximize the negatively charged zeta potential value while minimizing the hydrodynamic size and PDI of the dependent variable. The optimum levels of actual factors and their interaction effects on

Table 2
Outline of the experimental design matrix.

Run order	Space type	Independent variables (Factors)			Dependent variables (Responses)		
		X_1	X_2	X_3	Y_1	Y_2	Y_3
1	Axial	20	10	10	−40	118	0.264
2	Factorial	40	5	12	−46	118	0.26
3	Center	30	10	10	−49	160	0.284
4	Factorial	20	15	8	−30	184	0.341
5	Factorial	20	5	12	−35	105	0.241
6	Factorial	40	15	12	−55	173	0.29
7	Axial	30	15	10	−45	169	0.297
8	Factorial	40	5	8	−37	189	0.353
9	Factorial	40	15	8	−39	216	0.374
10	Axial	30	5	10	−42	115	0.269
11	Factorial	20	5	8	−35	176	0.324
12	Axial	30	10	8	−39	205	0.409
13	Center	30	10	10	−48	142	0.272
14	Axial	30	10	12	−46	119	0.262
15	Axial	40	10	10	−48	174	0.322
16	Factorial	20	15	12	−39	100	0.203
17	Center	30	10	10	−46	139	0.272

response were graphically identified by obtaining 3D response surface plots from the software. The mutual influence of two experimental factors on the responses was examined in the presence of the optimal constant value of the third factor in the 3D plots (Fig. 3a-i).

3.2.1. Zeta potential value

In a colloidal system, Zeta potential is a crucial parameter to determine the stability of suspension nanoscale particles. NPs with high zeta potential values are more stable and resistant to aggregation. The significance of the interaction between experimental components was evaluated based on plot surface changes. As shown in Fig. 3(a), the interaction effect of Bi and SBH concentrations was determined by preserving the sonication time at the optimum level of (12 min). Although the result shows that the zeta potential increased with both Bi and SBH concentrations and vice versa, Bi concentration influenced more. However, a weak interaction exists between the two concentrations on the zeta potential at lower sonication times. Fig. 3(b) shows a weak correlation effect between the Bi concentration and the sonication time on the zeta potential while keeping SBH constant at its minimum of 5 ml. However, this correlation became high when the SBH concentration was held constant at 15 ml. Fig. 3(c) depicts the interaction of sonication time and concentration of SBH on the zeta potential when the concentration of Bi is held constant at 40 ml. The results demonstrate that the zeta potential was also increased as the SBH concentration and sonication time increased. However, the effect of sonication time on the Zeta potential was the highest.

3.2.2. Hydrodynamic size and PDI

The hydrodynamic size and PDI are important properties of NPs for their biomedical applications. The hydrodynamic size of NPs impacts their half-life, biodistribution, and cellular internalization, whereas the PDI estimates the average uniformity of the NPs' suspension. The size of Fe_3O_4@Bi NPs varied between 100 and 216 nm. As shown in Table 3, the investigated variables significantly ($p < 0.05$) influenced the hydrodynamic size and PDI, however, the effect of SBH concentration on PDI was not significant. Fig. 3(d, g) illustrates the strong interaction impact of Bi and SBH concentrations on the hydrodynamic size and PDI, respectively. Decreasing both concentrations reduced the hydrodynamic size and PDI while maintaining the same sonication time. The effect of the correlation between Bi concentration and sonication time on the hydrodynamic size and PDI is shown in Fig. 3(e and h), respectively. The hydrodynamic size and PDI greatly decreased with an increase in sonication time and a decrease in Bi concentration. Similarly, by increasing the sonication time and decreasing SBH concentration the decrease in hydrodynamic size and PDI was observed as shown in Fig. 3(f and i), respectively. However, this interaction was weak on the PDI of the NPs.

It is evident from the comparative and graphical analysis that the sonication time had the highest significant effect on all of the three responses. However, the SBH concentration had the lowest effect. This implies that a minimum amount of reducing agent ($NaBH_4$) and maximum sonication time was required to produce highly stable and small hydrodynamic size Fe_3O_4@Bi NPs.

3.3. Optimization of factors and validation of models

Design Expert Software used a desirability function to perform numerical optimization. The goals for optimizing NPs were minimum SBH concentration, maximum sonication time, and maximum Bi concentration to obtain smaller hydrodynamic size, lower PDI, and higher zeta potential values. Different independent variables were found in 42 unique solutions, and the solution with the highest possible desirability

Table 3
(a) ANOVA results for factors (independent variables).

Responses	Factors	Sum of Squares	DF	Mean Square	F-value	*p*-value	Significant
Y_1 (Zeta Potential)	X_1	212.83	1	212.83	120.36	<0.0001	****
	X_2	17.34	1	17.34	9.8	0.0166	*
	X_3	170.02	1	170.02	96.15	<0.0001	****
	X_1X_2	17.6	1	17.6	9.95	0.016	*
	X_1X_3	32.27	1	32.27	18.25	0.0037	**
	X_2X_3	31.73	1	31.73	17.95	0.0039	**
	$(X_1)^2$	8.53	1	8.53	4.83	0.064	–
	$(X_2)^2$	12.21	1	12.21	6.9	0.034	*
	$(X_3)^2$	28.61	1	28.61	16.18	0.005	**
Y_2 (Hydrodynamic size)	X_1	3478.23	1	3478.23	14.79	0.002	**
	X_2	1946.03	1	1946.03	8.27	0.013	*
	X_3	12638.02	1	12638.02	53.73	<0.0001	****
Y_3 (PDI)	X_1	0.0056	1	0.0056	26.80	0.0002	***
	X_2	0.0008	1	0.0008	3.73	0.0757	–
	X_3	0.0251	1	0.0251	120.76	<0.0001	****

(b) ANOVA results for models of modified Fe_3O_4@Bi NPs.

Responses	R^2	Adj. R^2	Pred. R^2	Adeq. Precision	F-value	*p*-value	Lack of Fit p-value
Y_1	0.9807	0.9558	0.9089	23.9476	39.46	<0.0001	0.5643
Y_2	0.8552	0.8218	0.7250	18.3209	25.60	<0.0001	0.3842
Y_3	0.9209	0.9026	0.8673	23.5937	50.43	<0.0001	0.1804

Note 1: "****" $p < 0.0001$; "***" $0.0001 \leq p < 0.001$; "**" $0.001 \leq p < 0.01$; "*" $0.01 \leq p < 0.05$; "–" $p \geq 0.05$.
Note 2: DF is the degree of freedom.

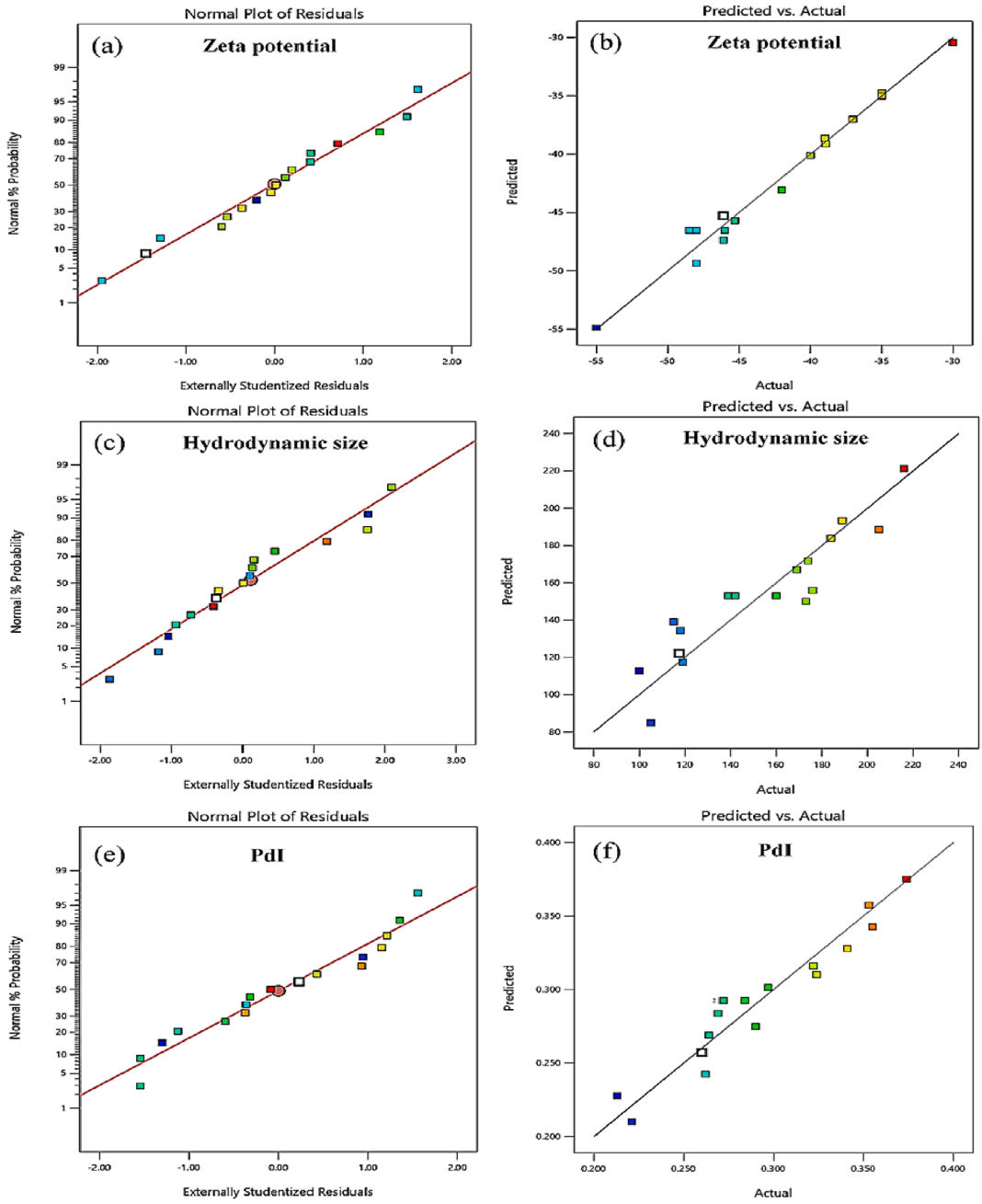

Fig. 2. Diagnostics of statistical models: (a, c, and e) normal plot of residuals and (b, d, and f) predicted versus actual values for the responses.

value was chosen as the optimized synthesis condition. As shown in Fig. 4, the optimized factors were found to be 40 ml, 5 ml, and 12 min for Bi concentration, SBH concentration, and sonication time, respectively, while the predicted values for responses were found to be −45 mV, 122 nm, and 0.257 for zeta potential, hydrodynamic size, and PDI, respectively.

The model's suitability for predicting response values was evaluated utilizing optimized synthesis conditions. Validation of optimized preparation conditions was accomplished by conducting experiments under optimal conditions. Using these predicted values, the potential for the responses has been improved experimentally. The experimental values for the zeta potential, hydrodynamic size, and PDI were found to be −47.1 mV, 125 nm, and 0.281, respectively. The predicted and experimental response values were very close. There was little difference between the values that can be attributed to the experimental conditions (Table 4).

3.4. Characterization of the optimized Fe_3O_4@Bi NPs

3.4.1. XRD analysis

The crystallinity and structure of the produced NPs were analyzed through the XRD technique. The XRD patterns of Fe_3O_4 NPs and Fe_3O_4@Bi composite NPs are presented in Fig. 5a and b. As shown in Fig. 5(a), seven main characteristic peaks were observed in the XRD of Fe_3O_4 NPs at $2\theta = 30.27°$, 35.57°, 43.23°, 53.63°, 57.29°, 62.95°, and 74.48°, respectively correspond to (220), (311), (400), (422), (511), (440), and (533) crystal planes (*hkl*), which could be well-indexed to the cubic structure of magnetite (Fe_3O_4) (JCPDS, Ref. No. 01-075-0033) [15]. However, as shown in Fig. 5(b), only five main diffraction peaks of Fe_3O_4 NPs were observed in the XRD pattern of the Fe_3O_4@Bi NPs at $2\theta = 30.19°$, 35.64°, 43.25°, 57.29°, and 62.95° correspond to (220), (311), (400), (511), and (440) crystal planes, respectively. The XRD pattern of Fe_3O_4@Bi NPs exhibited characteristic peaks for Fe_3O_4 NPs as

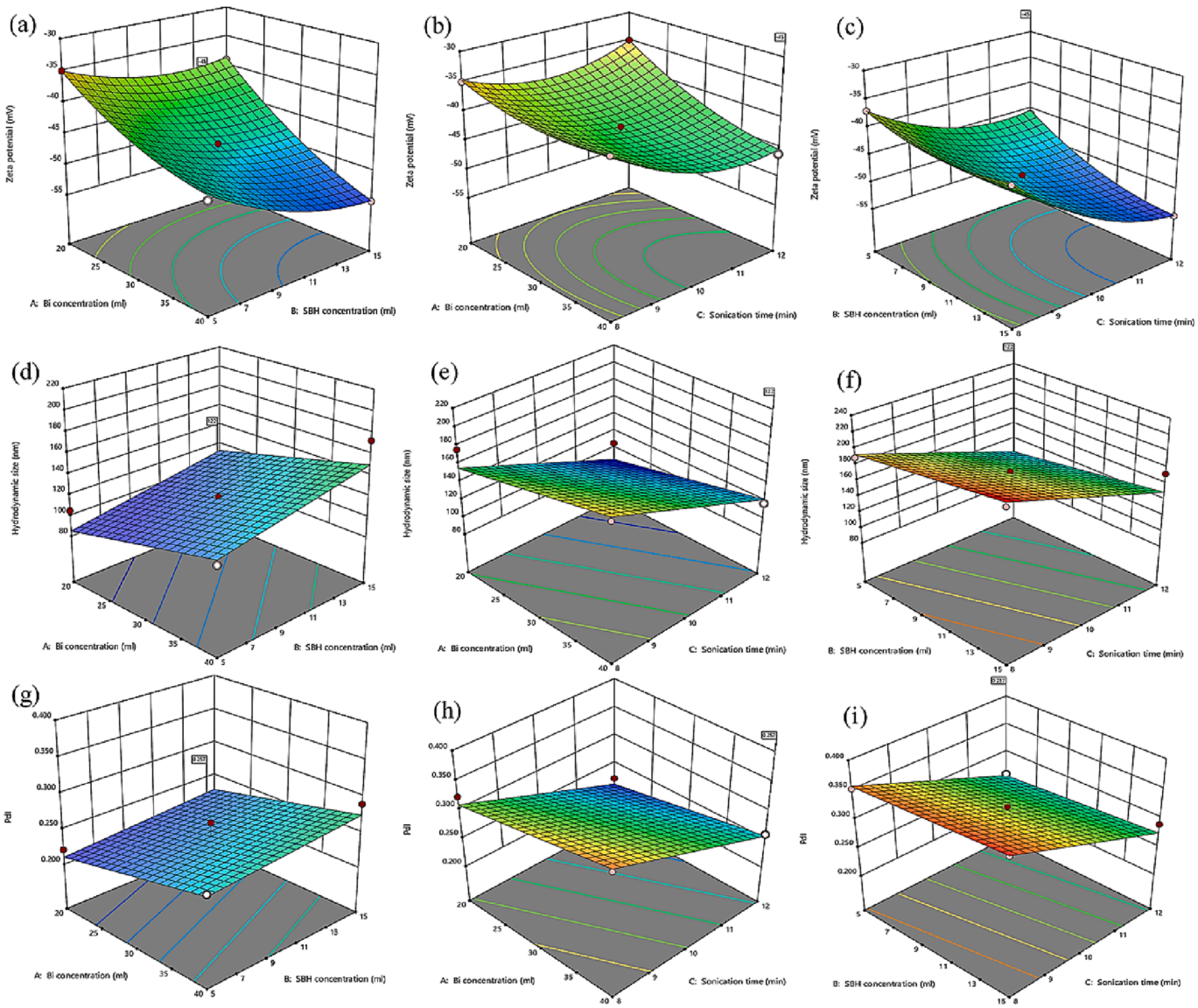

Fig. 3. 3D response surface plots showing mutual interaction and individual effects of independent factors on responses of the synthesized Fe_3O_4@Bi NPs: (a, d, g) 3D plot of Bi concentration vs concentration of SBH while keeping sonication time constant, (b, e, h) 3D plot of Bi concentration vs sonication time with constant SBH concentration, and (c, f, i) 3D plot of SBH concentration vs sonication time with Bi concentration held constant.

well as Bi NPs. The diffraction peaks at 2θ = 22.44°, 27.13°, 37.94°, 39.64°, 45.94°, 48.72°, 59.78°, 64.47°, 67.48°, 70.84 and 76.47° (Fig. 5b) respectively correspond to (003), (012), (104), (110), (113), (202), (107), (122), (018), (214), and (303) planes, indicate the presence of Bi NPs as a shell in the composition of Fe3O4@Bi nanocomposites. The peaks match the planes of the Bi rhombohedral phase (JCPDS, Ref. no. 00-044-1246) [43]. As shown in Fig. 5 and presented in Table 5, the slightly shifted of the three appeared peaks and the disappearance of the other peaks of Fe_3O_4 in the XRD patterns of Fe_3O_4@Bi NPs are attributed to 1) the incorporation and grafting of heavy Bi layer on their surfaces, and 2) probably the sonication period [31], thereby affecting their crystallinity. Broadening of the appeared peaks of Fe_3O_4 NPs and decreasing their intensities were also observed in the XRD pattern of the composite NPs, thereby confirming the successful coating and formation of the Fe_3O_4@Bi NPs. However, the shift in d-spacing values has not been observed in any of the NPs' crystal planes (Table 5). The inter-planar spacing (d-spacing) values were determined using Eq. (5). These findings are consistent with previous studies [22,24]. The peaks of full-width half maximum (FWHM) at the crystal planes have been calculated and exerted to normalize the XRD pattern of both Fe_3O_4 and Fe_3O_4@Bi NPs, and the average crystallite size has been determined to be approximately 11.3 nm and 19.7 nm, respectively, using the Debye-Scherrer equation (Eq. (6) [15]. The XRD corroborates the successful functionalization of Fe_3O_4 NPs as core via coating their surface with crystalline Bi shell by ultrasonic irradiation under the optimum sonication time and power. Although the Fe_3O_4 NPs were exceptionally coated with Bi NPs, the Bi layer, as well as the optimal sonication time and power (12 min, 40 W), affected their crystalline structure.

$$d_{hkl} = \frac{\lambda}{2sin\theta} \tag{5}$$

where hkl denotes Miller indices, λ represents the X-ray wavelength of CuKα = 1.54060 A°, and θ represents Bragg's angle in degrees, half of 2θ.

And the following is the Debye-Scherrer equation Eq.:

$$D = \frac{K\lambda}{\beta cos\theta} \tag{6}$$

where D represents the crystallite size, K is the shape factor (Scherrer constant, 0.9), λ denotes the X-ray wavelength for Cu kα, β is the FWHM,

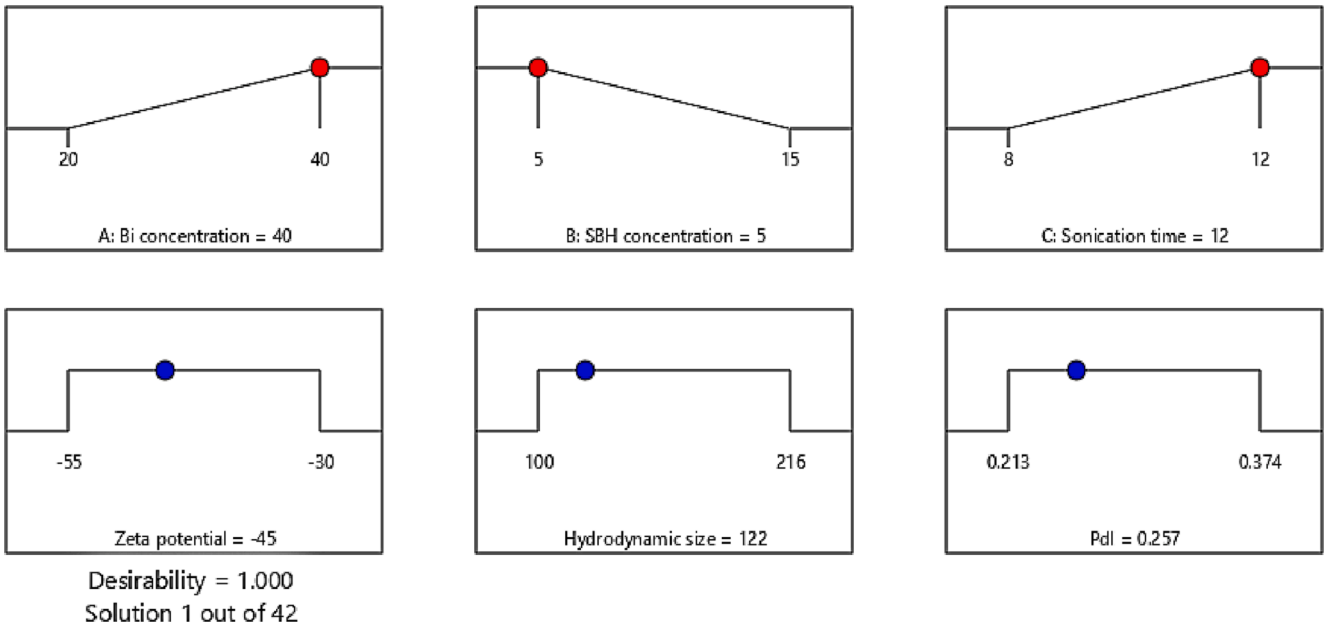

Fig. 4. Desirability ramps showing the optimized values of independent variables for improving the zeta potential, hydrodynamic size, and PDI of the NPs.

Table 4
Optimum actual factors, predicted, and experimental values of responses at optimized conditions.

Factors	Optimal actual levels		
Bi concentration (ml)	40		
SBH concentration (ml)	5		
Sonication time (min)	12		
Responses	Predicted values	Experimental values	Differences (%)
Zeta potential (mV)	−45.29	−47.10	3.99
Hydrodynamic size (nm)	122.18	125.40	2.64
PDI	0.257	0.281	9.33

and θ represents the diffraction angle.

3.4.2. TEM analysis

The particle size and size distribution of the produced NPs were analyzed by the TEM technique. Fig. 6 illustrates the TEM images and particle size distribution of Fe_3O_4 NPs and Fe_3O_4@Bi NPs. As seen in Fig. 6(a, c), the majority of Fe_3O_4 NPs have spherical shapes, small sizes, and are monodispersed with a particle size distribution ranging from 5 nm to 20 nm and an average particle size of about 11.7 nm. The TEM micrograph and size distribution Fe_3O_4@Bi composite NPs are illustrated in Fig. 6 (b, d). The results showed that the nanocomposites were semi-spherical and homogeneous, and their size distribution ranged from 9 to 29 nm with an average diameter of about 19.5 nm. The TEM image demonstrates that the size of Fe_3O_4 NPs increased from 11.7 to 19.5 nm after being coated with the Bi layer. This increase in the average particle size of the Fe_3O_4 NPs by roughly 7.8 nm indicates the incorporation and grafting of the Bi NPs onto the surface of Fe_3O_4 NPs, resulting in the formation of Fe_3O_4@Bi composite NPs. The TEM result revealed that the ultrasound can rapidly graft the Bi NPs on Fe_3O_4 NPs and produce a homogeneous, uniform, and narrow size distribution of Fe_3O_4@Bi nanocomposites in a core@shell structure with a limited short sonication period of 12 min.

3.4.3. FESEM and EDX analysis

The morphology, elemental compositions, and weight with atomic percentages of Fe_3O_4 and Fe_3O_4@Bi NPs are presented in Fig. 7. The FESEM images further confirmed that the Fe_3O_4 NPs were spherically formed and monodispersed with small particle sizes (Fig. 7 (a)). Fe_3O_4@Bi NPs also show larger particle sizes and uniform distributions with the majority of semi-spherical shapes in the FESEM (Fig. 7 (b)).

The EDX spectra were employed for quantitative elemental analysis of magnetite and bismuth-coated magnetite NPs. As seen in Fig. 7 (c) and (d), Fe_3O_4 NPs exhibited elemental peaks corresponding to Fe, O, and C, whereas Fe_3O_4@Bi NPs exhibited extra Bi peaks, respectively. The presence of Bi in the spectra of the coated NPs confirms the surface functionalization of Fe_3O_4 NPs with a Bi shell to form Fe_3O_4@Bi NPs. Existing elements C, O, Fe, and Bi were found in the core@shell NPs at weight percentages of 5.93, 18.1, 40.99, and 34.99%, respectively, whereas their atomic percentages were found to be 19.54, 44.78, 29.05, and 6.63%. As a result, the FESEM and EDX affirmed that the Bi shell was highly conjugated on the surface of Fe_3O_4 NPs under the influence of the acoustic cavitation process from ultrasonic irradiation at the optimum sonication time and power.

3.4.4. RAMAN analysis

The Raman spectrum of *Sumac* extract, *Sumac*-Bi NPs, *Sumac*-Fe_3O_4 NPs, and Fe_3O_4@Bi composite NPs are respectively displayed in Fig. 8 (a). *Sumac* extract exhibited only a single broad band. However, the Raman spectrum of *Sumac*-Bi NPs showed two prominent peaks at approximately 123 cm^{-1} and 307 cm^{-1}, both of which correspond to unique Bi-O stretches associated with the β-phase Bi_2O_3 [44]. In addition, multiple peaks have been identified in the Raman spectra of *Sumac*-Fe_3O_4 NPs, as shown in Fig. 8a (black line). The spectra displayed a peak at 1298 cm^{-1} that corresponded to the D-band of *Sumac*-Fe_3O_4 NPs [45]. This could be owing to the existence of imperfections on the surface of NPs. The characteristic bands for Fe_3O_4 are located at approximately 670, 538, and 306 cm^{-1} [46]. However, three peaks can be observed at around 399, 493, and 600 cm^{-1}, which match the vibration modes of the Fe-O bonds in Fe_3O_4 NPs [45]. Compared to the reported values, these shifts in the spectrum of *Sumac*-Bi and *Sumac*-Fe_3O_4 NPs can be attributed to the incorporation of the *Sumac* extracts. The peaks at 220 and 285 cm^{-1} are attributable to the oxidation reaction that took place during the Raman experiment; however, the peak at around 285 cm^{-1} has not been observed and the peak at 220 cm^{-1} has weakly appeared, shifted to 238 cm^{-1} in the Raman pattern of Fe_3O_4@Bi NPs, indicating

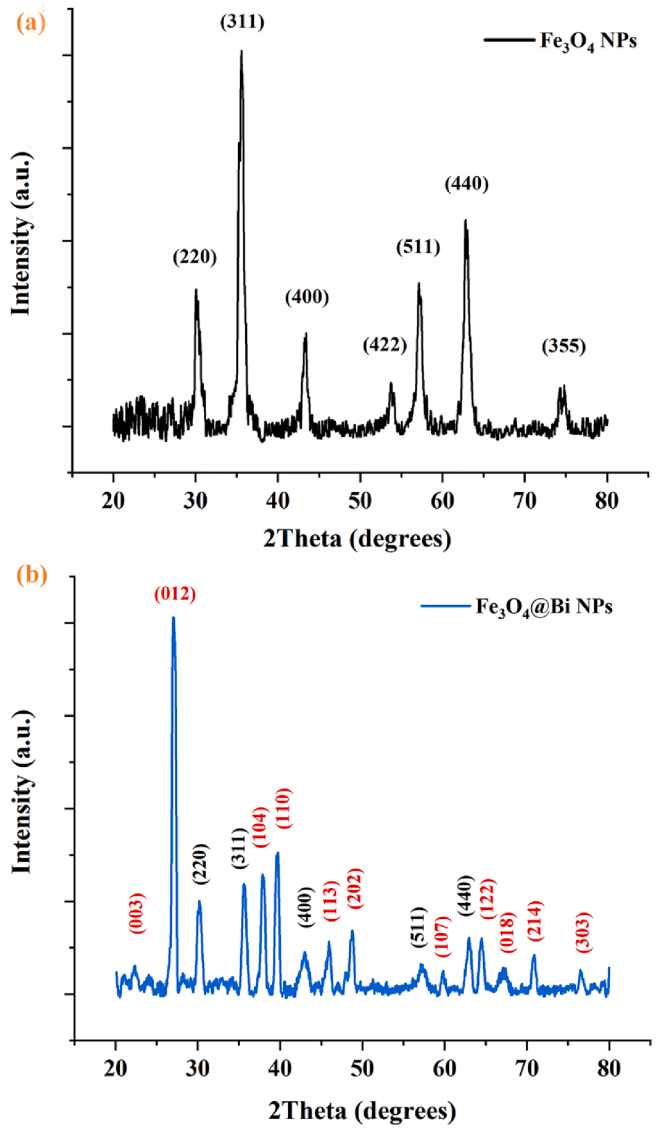

Fig. 5. The XRD Patterns of (a) Fe_3O_4 NPs and (b) Fe_3O_4@Bi NPs.

that the core NPs are indeed Fe_3O_4 and have not been oxidized. Nevertheless, peaks at 123 and 307 cm^{-1} in the spectrum of Bi NPs and at 399, 493, and 600 cm^{-1} in the spectrum of Fe_3O_4 NPs were shifted to around 124, 308, 473, 499, and 685 cm^{-1}, respectively. These shifts can be due to the incorporation of Bi NPs into the Fe_3O_4 NPs under ultrasonic irradiation conditions and functionalizing the formation of nanocomposites by covering their surface with *Sumac* extracts. The Raman results revealed that the formation of Fe_3O_4@Bi NPs is a composite of both Bi and Fe_3O_4; nevertheless, the wide shifts at approximately 473 cm^{-1} and 685 cm^{-1} indicates that the structure of the Fe_3O_4 NPs was influenced by grafting of the Bi layer under the impact of ultrasonic irradiation duration [21,31]. The findings agree with those obtained from the XRD analysis of the nanocomposite.

3.4.5. FTIR analysis

The role of organic molecules and functional groups of *Sumac* extract solution in the composition of Fe_3O_4@Bi nanocomposites was determined by FTIR analysis. Fig. 8(b) displays the FTIR spectra of Fe_3O_4 NPs (black line), *Sumac* extract (light red line), and the nanocomposite (green line) between 4000 and 400 cm^{-1}. Peaks at 3400–3000 cm^{-1}, 1710 cm^{-1}, and 1650–1450 cm^{-1} in the FTIR spectrum of *Sumac* extract are ascribed to the O-H stretching vibration of the hydroxyl group of

Table 5
The X-ray powder scattering calculated data for Fe_3O_4 NPs and Bi and Fe_3O_4 in the Fe_3O_4@Bi structure.

Sample	hkl	2θ°	FWHM (θ°)	d (nm)	Intensity (a. u)
Fe_3O_4 NPs	220	30.27	0.6387	0.295	28.5
	311	35.57	0.7511	0.252	100.0
	400	43.23	0.9901	0.209	17.6
	422	53.63	0.7323	0.171	10.7
	511	57.29	0.8332	0.161	18.2
	440	62.95	0.8401	0.148	27.9
	533	74.48	0.7999	0.127	8.3
Iron oxide in Fe3O4@Bi NPs	220	30.19	0.6202	0.296	20.6
	311	35.64	0.7573	0.252	22.4
	400	43.25	0.9777	0.209	8.8
	422	–	–	–	–
	511	57.29	0.8442	0.161	6.5
	440	62.95	0.8520	0.148	12.4
	533	–	–	–	–
Bismuth in Fe3O4@Bi NPs	003	22.44	0.4993	0.396	8.5
	012	27.13	0.3051	0.328	81
	104	37.94	0.3420	0.237	23.2
	110	39.64	0.3626	0.227	26.8
	113	45.94	0.8687	0.197	7.8
	202	48.72	0.4035	0.187	9.6
	107	59.78	0.8241	0.155	5.1
	122	64.47	0.5467	0.144	9.8
	0.18	67.48	0.3979	0.1399	5.5
	214	70.84	0.4488	0.133	7.4
	303	76.47	0.4984	0.124	5.8

phenolic compounds, C = O stretching vibration of the carbonyl group of carboxylic acid, and aromatic ring stretching vibration, respectively. C–N stretching absorptions are observed between 1200 and 1350 cm^{-1} for aromatic amines and between 1000 and 1300 cm^{-1} for aliphatic amines [15]. Compared to the spectrum of Fe_3O_4 NPs (black line), the peaks at 3243 cm^{-1}, 1589 cm^{-1}, 1357 cm^{-1}, 1205 cm^{-1}, and 1074 cm-1 are respectively shifted to 3212 cm^{-1}, 1575 cm^{-1}, 1340 cm^{-1}, 1195 cm^{-1}, and 1070 cm^{-1} in the IR spectrum of Fe_3O_4@Bi NPs. These shifts, which correspond to high intensities, are probably attributable to the –OH group of hydroxyl and C = O group of carbonyl, C–C of the aromatic ring, C–H bending of alkanes or C–C the stretch of aromatics, and –CH and –CH2 vibrations of aliphatic hydrocarbons, respectively [15]. The prominent peaks found between 400 and 690 cm1 in the spectra of Fe_3O_4 NPs are attributed to the M−O vibration, which corresponds to the iron oxide's Fe–O bonds. The sharp peak of the Fe–O band at 511 cm^{-1} was shifted to 553 cm^{-1} in the spectrum of the composite NPs. Thus, the carboxyl and amine groups of organic biomolecules, including tannins, flavonoids, and other phenolic compounds present in the *Sumac* extract solution [16], were incorporated and absorbed onto the surface of the nanocomposite and played crucial roles in stabilizing and functionalizing the Fe_3O_4@Bi NPs.

3.4.6. UV–visible spectral analysis

The optical absorption property of Fe_3O_4@Bi NPs is one of the essential characteristics for monitoring the formation and evaluating the optical activity of the composite NPs, in addition to identifying the presence of the coated Bi outer shell. UV–visible absorption involves interactions between incident light and the outer electrons of atoms or molecules on the surface of the NPs in a solution, which results in the absorption of radiant energy and transitions to high energy levels known as surface plasmon resonance (SPR), which displays the absorption in a spectrum [47,48]. In this study, SPR has been employed to investigate modifications in the electronic configuration of the NPs caused by surface effects. Fig. 8(c) illustrates the UV–visible absorption of the produced NPs in the spectra ranges of 200–700 nm at room temperature. The Fe_3O_4 NPs show a broad absorption band at about 380 nm (black spectra). Previous studies demonstrated that the magnetite NPs exhibited absorption spectra from 350 to 400 nm [49] and 400–420 nm [50]

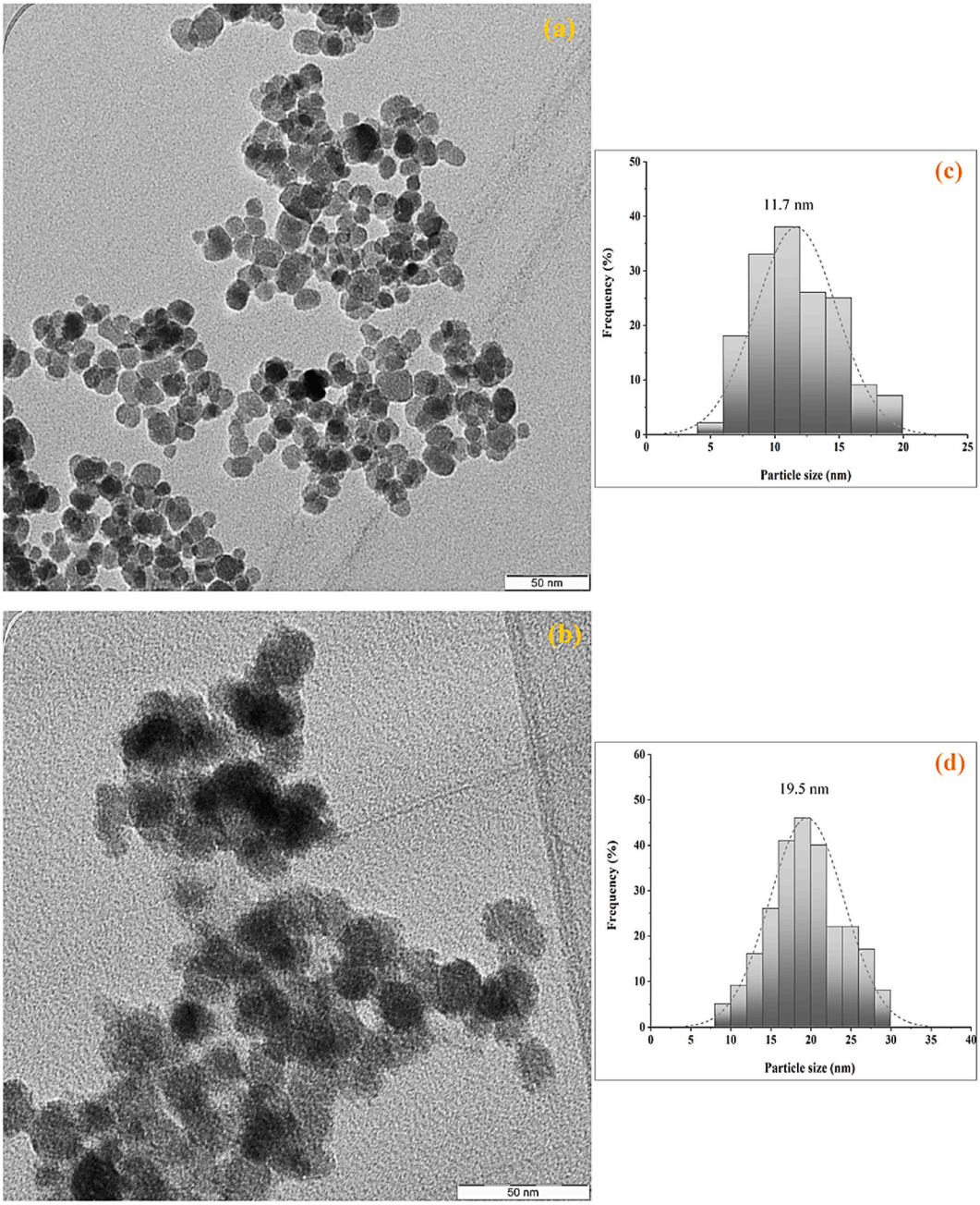

Fig. 6. TEM micrographs with scale-bare of 50 nm and size distribution histogram of Fe_3O_4 NPs (a, c) and Fe_3O_4@Bi NPs (b, d).

with broad bands. Nevertheless, this peak can be shifted to lower wavelengths when the magnetite NPs are functionalized with biocompatible compounds [50]. The absorption band of our Fe_3O_4 NPs spectra is in between the reported values. However, after coating with Bi, the Fe_3O_4@Bi NPs exhibited a prominent absorption peak of about 321 nm (red spectra), showing the successful development of Bi shell on Fe_3O_4 core NPs. The appearance of the new peak at 321 nm is thought to be originating from the absorption property of the deposited Bi layer formed on the Fe_3O_4 NPs. The UV–Vis result corroborates the improvement of the optical property of Fe_3O_4 NPs through grafting their surface with elemental BiNPs to create a new form of Fe_3O_4@Bi NPs under the influence of the acoustic cavitation process from the ultrasound.

3.4.7. *Magnetization*

The Magnetic characteristics of the synthesized Fe_3O_4 and Fe_3O_4@Bi NPs were investigated by VSM at room temperature. The hysteresis loops and the saturation magnetization (*Ms*) results of the NPs as a function of the applied magnetic field between −15,000 Oe and + 15,000 Oe are displayed in (Fig. 8d). The result of the VSM magnetization curves demonstrated that Fe_3O_4 NPs and Fe_3O_4@Bi NPs are superparamagnetic, with *Ms* values of 132.33 emu/g and 92.19 emu/g, as well as very low coercivities of 14.07 Oe and 12.66 Oe, respectively. Our group recently reported the superparamagnetic magnetite NPs with an extremely high *Ms* value [15]. However, the VSM results of our current study indicate that the incorporation of bismuth influenced the last *Ms* value of the nanocomposites. This reduction in the *Ms* value of the Fe_3O_4@Bi NPs is probably due to the coating of the Bi layer as a shell on the surface of Fe_3O_4 NPs and the result is consistent with those previously reported [20–23]. Hence, Bi as a non-toxic and inexpensive heavy metal exhibits a diamagnetic behavior [19]. Although, the Bi shell decreases the *Ms* of Fe_3O_4@Bi NPs, however, their value (92.19 emu/g)

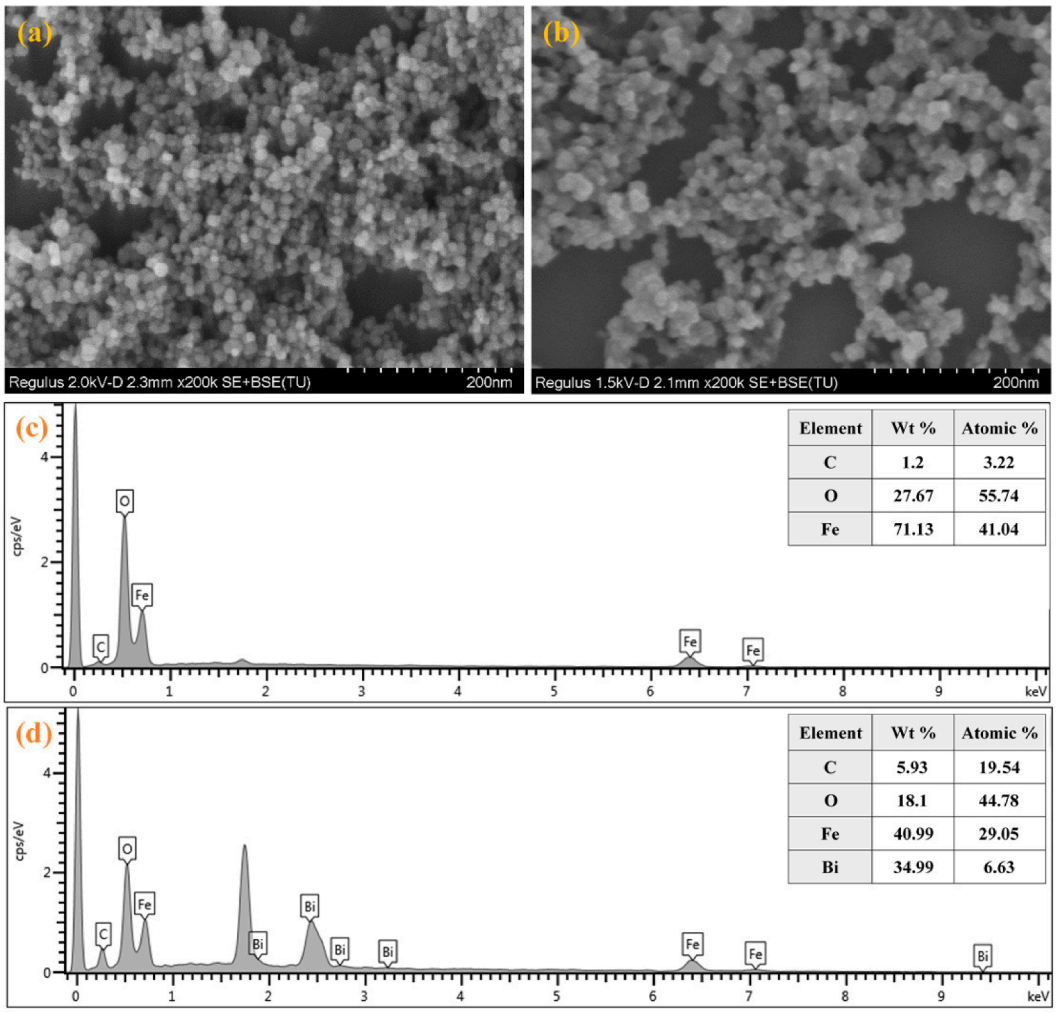

Fig. 7. FESEM image with scale-bare of 200 nm, EDX spectra, and elemental quantification of (a, c) Fe_3O_4 NPs, and (b, d) Fe_3O_4@Bi NPs.

at room temperature is still higher than that of bulk Fe_3O_4 (86 emu/g) [51]. This is probably due to 1) the core@shell structure of the nanocomposite that relatively retains the properties of the core NPs [6]. 2) Synthesis of the core Fe_3O_4 NPs via the green-assisted method using *Sumac* extracts resulted in the creation of the NPs with excessively large *Ms* [15]. Subsequently, utilizing this Fe_3O_4 core as a seed template and growing the Bi shell NPs on their surface was not significantly affected the *Ms* of the last product. Unlike a reported method that prepared Bi/Fe_3O_4 hybrid NPs through the co-precipitation of iron and bismuth salts in one-pot synthesis procedure which resulted in the formation of the nanohybrid with extremely low *Ms* value and non-superparamagnetic [21], our core@shell structure of the nanocomposite relatively prevented the *Ms* value of the core NPs with superparamagnetic form. It can be concluded that the ultrasonic-assisted technique with sonication time and power up to 12 min and 40 W had no effect on the *Ms* value of the functionalized NPs and that the reduction in *Ms* can be attributable to the Bi shell coating. Due to the combined characteristics of Bi and Fe_3O_4 NPs, sonochemically synthesized Fe_3O_4@Bi composite NPs are probably advantageous for a wide range of biomedical applications.

3.4.8. Stability and hydrodynamic size

The stability and uniform dispersion of NPs in a biological environment are crucial for their successful use in biomedical applications. The zeta potential, hydrodynamic size, and PDI of the colloidal suspension of Fe_3O_4 and Fe_3O_4@Bi NPs were determined using DLS. The stability of the colloidal suspension of both NPs solutions was determined by measuring the electrostatic potential on the ionic surface of the NPs using the zeta potential. The colloidal solution rapidly aggregates and precipitates with a zeta potential of 0 to ± 5 mV. Zeta values ranging between ± 10 and ± 30 mV indicate a delicate dispersion. However, the zeta potential in the ranges ± 30 to ± 40 mV and ± 40 to ± 60 mV exhibit moderately stable and highly stable, respectively [6]. As shown in Fig. 9(a) and (b), the zeta potential value and hydrodynamic size of Fe_3O_4 NPs were found to be –33.5 mV and 98.4 nm (red lines), while these values were found to be −47.1 mV and 125.4 nm (green lines) for Fe_3O_4@Bi NPs, respectively. The increase in the zeta potential value of the Fe_3O_4@Bi NPs can be attributed to the influence of the ultrasonic irradiation with the optimized sonication time and power [31] in producing the BiNPs as a coated shell. In addition, the use of *Sumac* extract as stabilizing agent improved the zeta potential of Fe_3O_4@Bi NPs via adsorbing carboxyl and amine functional groups on the surface of the NPs, resulting in extremely negative surface loads and enhancing their stabilities [15]. These functional groups of biomolecules, which highly exist in *Sumac* extract solution enable particles to generate a high surface charge under sonochemical conditions, increasing the zeta potential and electrostatic repulsion force between particles and preventing particle attraction and collision. This is similar to previously reported works that enhanced the stability of NPs through coating with chitosan solution and increased the zeta potential values by loading positive electrical charges on their surface [31,52]. Moreover, the increase in the hydrodynamic size of the composite NPs was due to the modification of their surface caused by the grafting of the Bi layer. However, the PDI result revealed

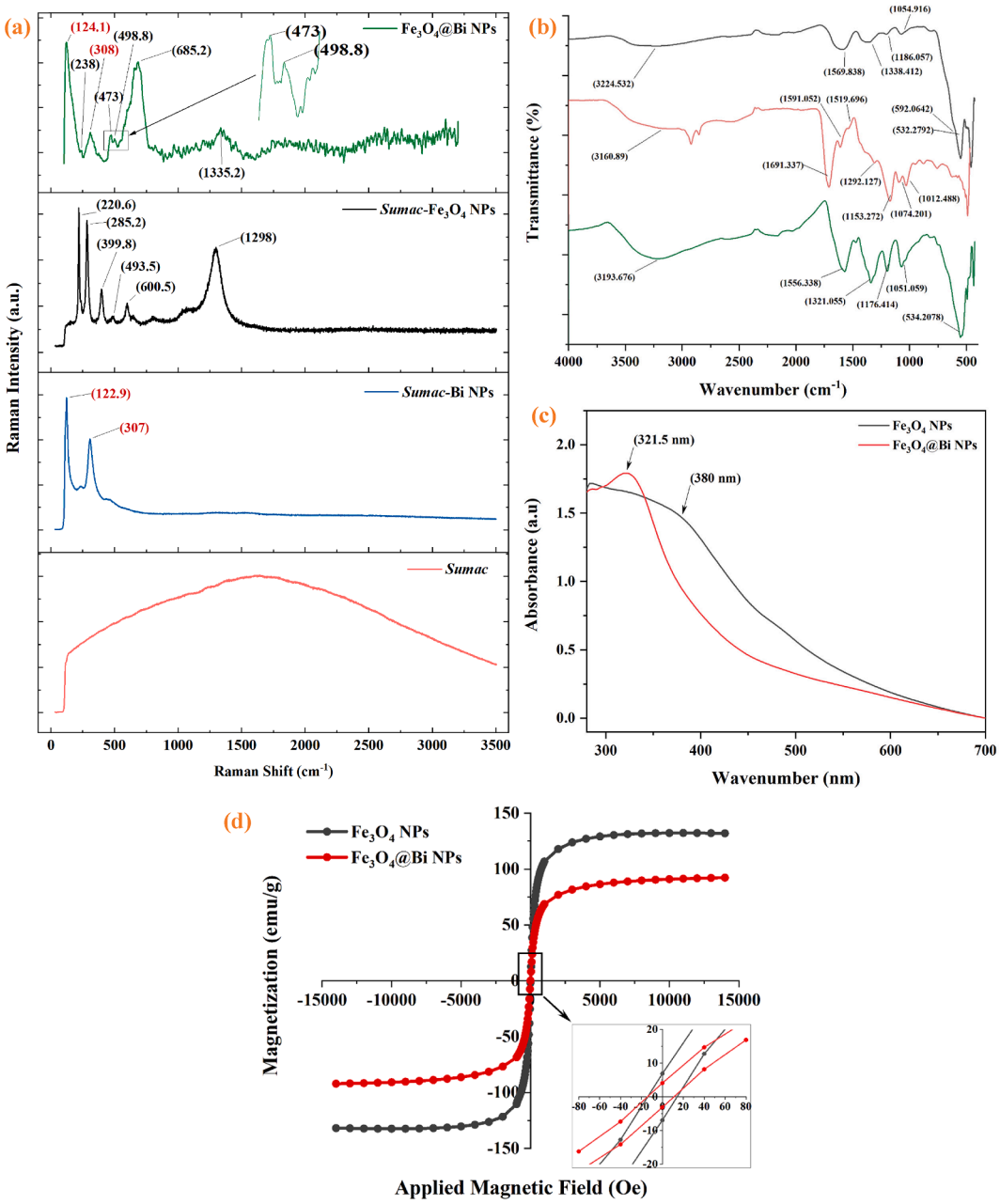

Fig. 8. (a, b) Raman spectroscopy and FTIR spectrum of Fe_3O_4 NPs (black line), *Sumac* extract (light red line) and Fe_3O_4@Bi NPs (green line), as well as a Raman spectra of Bi NPs (blue line) and (c, d) UV–visible spectra and magnetization curve of Fe_3O_4 NPs (black lines) and Fe_3O_4@Bi NPs (red lines), respectively.

that Fe_3O_4@Bi NPs had a narrow particle size distribution (0.281). The results indicate that the sonochemical approach produced exceptionally stable nanocomposites with a zeta potential value of −47 mV in a high range between ± 40 and ± 60 mV, which are considered to have the sufficient inter-particle electrostatic repulsive force to accomplish such excellent colloidal stability [6,32]. This value is significantly higher than that of the similar reported works synthesized by conventional methods [20,21,23].

3.5. Cytotoxicity of Fe_3O_4@Bi NPs

The toxicity of the developed NPs is an essential evaluation issue for future biomedical applications. In this study, human embryonic kidney cells were selected for two main reasons: (a) according to a previous study, the kidney is one of the organs, after the spleen, that accumulated the highest amount of bismuth and iron two hours after Bi/Fe_3O_4 (Bi-30) NPs injection into C57BL/6J mice, with the bismuth content on the kidneys being much more than that of iron. In addition, it has been found that the excretion of bismuth in urine is significantly higher than that of iron [21]; (b) the exposure concentration of the Bi NPs might also be related to the cytotoxicity reaction. It has been shown in specified concentrations that cytotoxicity studies are not affected by the type of cell being tested. The cytotoxicity of Fe_3O_4@Bi NPs has been evaluated in HEK-293 cells via a standard MTT assay at concentrations of (50–400 μg/ml) and incubation times of (24–72 h). As shown in Fig. 9(c), the viability of cells decreased with increasing the NPs concentrations and incubation durations, however, the cytotoxic effect of Fe_3O_4@Bi NPs on HEK-293 cells has not been observed at these ranges of concentration. The viability of the cells in percentage was found to be more than 80% at the highest of 400 μg/ml and longest incubation duration of 72 h, indicating the non-toxicity of the examined NPs. Previous studies have reported the non-toxicity of Bi/Fe composite NPs on different cell lines

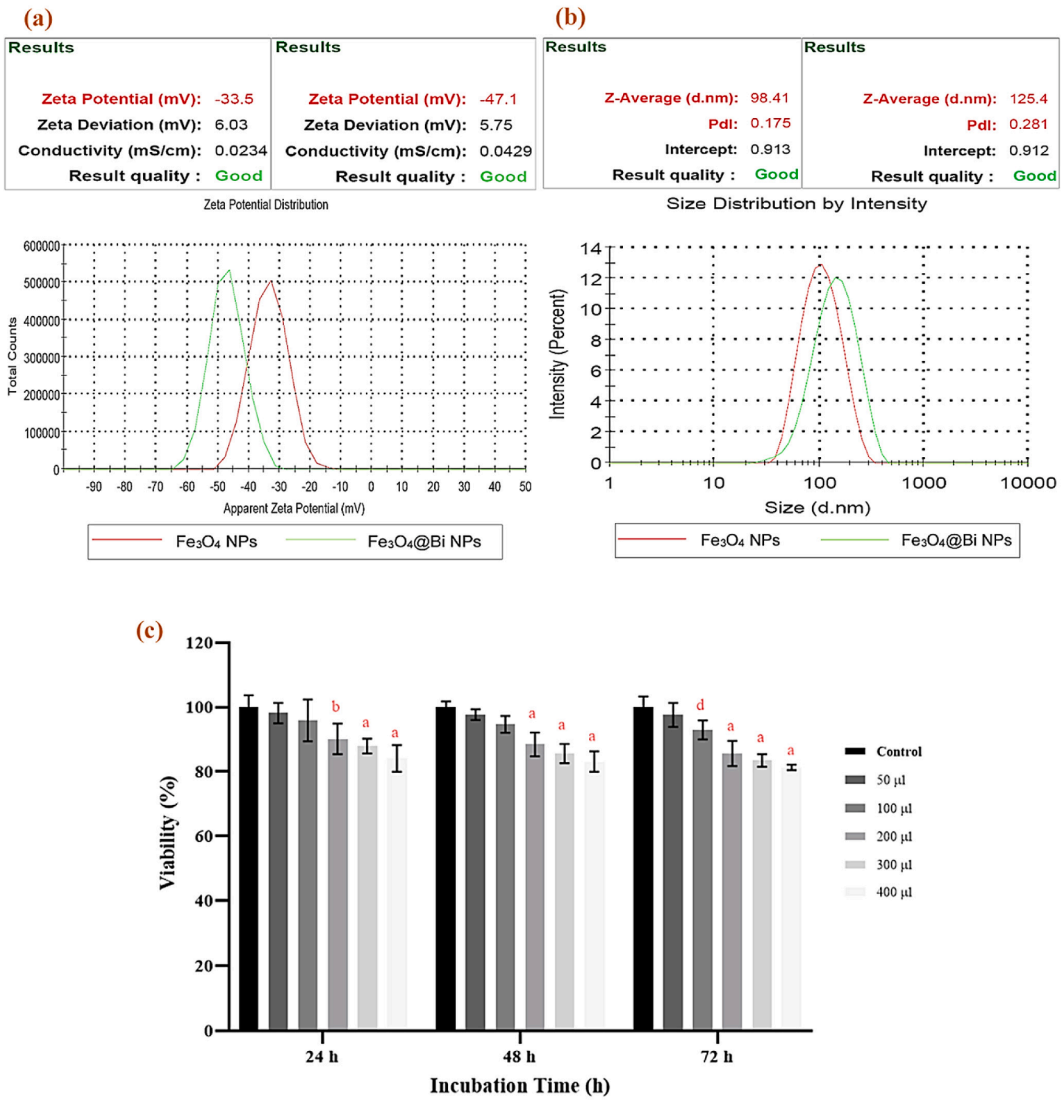

Fig. 9. (a, b) Zeta potential and hydrodynamic size of Fe_3O_4 NPs (red line) and Fe_3O_4@Bi NPs (green line), respectively, and (c) comparing the viability of cells at various NPs concentrations after 24, 48, and 72 h of incubation. The results were expressed in percentage versus the control (untreated) group, (mean ± SD, n = 4), using (Two-way ANOVA, Multiple Comparisons, Dunnett); a = $p < 0.0001$, b = $0.0001 \leq p < 0.001$, c = $0.001 \leq p < 0.01$, d = $0.01 \leq p < 0.05$, and "–" = $p \geq 0.05$.

at various concentrations and incubation durations [21–25]. Nanomaterials with 80% or higher cell viability are considered biologically compatible. This result confirmed the non-toxicity and biocompatibility of Fe_3O_4@Bi NPs and thus have the potential to be used in biomedical applications. Although, the Fe_3O_4@Bi nanocomposites exhibited no cytotoxicity towards HEK-293 cells; however, as this is a work in progress, additional in vitro and *in vivo* study is required to further determine their biocompatibility and biodegradability.

4. Conclusion

The rapid and facile synthesis of Fe_3O_4@Bi composite NPs has been accomplished through the sonochemical method. The ultrasound was assisted the growth of bismuth NPs on the surface of iron oxide NPs within 12 min sonication. Due to their critical role in biomedical applications, the stability, size, and size distribution of the produced nanocomposite were evaluated to establish highly biocompatible particles. The use of *Sumac* extract solution in the synthesis procedure enables the improvement of stability and biocompatibility of the nanocomposite. In addition, this study demonstrated that RSM is a useful technique for optimizing the synthetic conditions for the sonochemical production of Fe_3O_4@Bi NPs and exploring the relationship between the preparation parameters and the response variables. The results showed that the sonication time was the most influential factor that efficiently affected the responses. The optimized preparation conditions were determined based on numerical optimization using the desirability function. The nanocomposites were experimentally reproduced, and their physicochemical properties were characterized. The findings of this study enable the control of the optimum experimental conditions for the synthesis of the NPs with zeta potential, hydrodynamic size, and PDI of −47.1 mV, 125.4 nm, and 0.281, respectively. The results indicate that the application of ultrasonic irradiation in conjunction with the experimental design significantly functionalized the Fe_3O_4 NPs via coating with BiNPs, thereby generating a novel Fe_3O_4@Bi NPs with excellent properties including small particle sizes, highly stable, high magnetic properties, and biocompatible that probably has a potential for a wide range of biomedical applications.

Declaration of Competing Interest

The authors declare that they have no known competing financial interests or personal relationships that could have appeared to influence

the work reported in this paper.

Acknowledgments

We wish to extend our gratitude to the Universiti Sains Malaysia for providing us with the Research University Grant FRGS/1/2021/STG05/USM/02/6 in supporting this work.

References

[1] Y. Xiao, J. Du, Superparamagnetic nanoparticles for biomedical applications, J. Mater. Chem. B 8 (2020) 354–367, https://doi.org/10.1039/c9tb01955c.
[2] N. Zhu, H. Ji, P. Yu, J. Niu, M. Farooq, M. Akram, I. Udego, H. Li, X. Niu, Surface modification of magnetic iron oxide nanoparticles, Nanomaterials 8 (10) (2018) 810.
[3] J. Chai, Y. Ma, T. Guo, Y. He, G. Wang, F. Si, J. Geng, X. Qi, G. Chang, Z. Ren, R. Yu, L. Song, D. Li, Assembled Fe3O4 nanoparticles on Zn–Al LDH nanosheets as a biocompatible drug delivery vehicle for pH-responsive drug release and enhanced anticancer activity, Appl. Clay Sci. 228 (2022) 1–9, https://doi.org/10.1016/j.clay.2022.106630.
[4] E. Aram, M. Moeni, R. Abedizadeh, D. Sabour, H. Sadeghi-Abandansari, J. Gardy, A. Hassanpour, Smart and Multi-Functional Magnetic Nanoparticles for Cancer Treatment Applications: Clinical Challenges and Future Prospects, Nanomaterials 12 (2022) 3567, https://doi.org/10.3390/nano12203567.
[5] M.A. Dheyab, A.A. Aziz, P.M. Khaniabadi, M.S. Jameel, Potential of a sonochemical approach to generate MRI-PPT theranostic agents for breast cancer, Photodiagn. Photodyn. Ther. 33 (2021) 102177.
[6] M.A. Dheyab, A.A. Aziz, M.S. Jameel, Synthesis and optimization of the sonochemical method for functionalizing gold shell on Fe3O4 core nanoparticles using response surface methodology, Surf. Interfaces 21 (2020) 100647.
[7] M.D. Nguyen, H.-V. Tran, S. Xu, T.R. Lee, Fe3O4 nanoparticles: Structures, synthesis, magnetic properties, surface functionalization, and emerging applications, Appl. Sci. 11 (23) (2021) 11301.
[8] D. Tsamos, A. Krestou, M. Papagiannaki, S. Maropoulos, An Overview of the Production of Magnetic Core-Shell Nanoparticles and Their Biomedical Applications, Metals (Basel). 12 (4) (2022) 605.
[9] M. Vinyas, S.J. Athul, D. Harursampath, M. Loja, T. Nguyen Thoi, A comprehensive review on analysis of nanocomposites: From manufacturing to properties characterization, Mater. Res. Express 6 (9) (2019) 092002.
[10] M.A. Dheyab, A.A. Aziz, M.S. Jameel, O.A. Noqta, P.M. Khaniabadi, B. Mehrdel, Simple rapid stabilization method through citric acid modification for magnetite nanoparticles, Sci. Rep. 10 (2020), https://doi.org/10.1038/s41598-020-67869-8.
[11] B. Dutta, S. Checker, K.C. Barick, H.G. Salunke, V. Gota, P.A. Hassan, Malic acid grafted Fe3O4 nanoparticles for controlled drug delivery and efficient heating source for hyperthermia therapy, J. Alloy. Compd. 883 (2021) 160950.
[12] C. Chircov, R.E. Ştefan, G. Dolete, A. Andrei, A.M. Holban, O.C. Oprea, B.S. Vasile, I.A. Neacşu, B. Tihăuan, Dextran-Coated Iron Oxide Nanoparticles Loaded with Curcumin for Antimicrobial Therapies, Pharmaceutics. 14 (2022) 1057, https://doi.org/10.3390/pharmaceutics14051057.
[13] J.-Z. Sun, Y.-C. Sun, L. Sun, Synthesis of surface modified Fe3O4 super paramagnetic nanoparticles for ultra sound examination and magnetic resonance imaging for cancer treatment, J. Photochem. Photobiol. B Biol. 197 (2019) 111547.
[14] M. Magro, F. Vianello, Bare iron oxide nanoparticles: Surface tunability for biomedical, sensing and environmental applications, Nanomaterials 9 (2019), https://doi.org/10.3390/nano9111608.
[15] F.S. Braim, N.N.A. Nik Ab Razak, A.A. Aziz, M.A. Dheyab, L.Q. Ismael, Rapid green-assisted synthesis and functionalization of superparamagnetic magnetite nanoparticles using Sumac extract and assessment of their cellular toxicity, uptake, and anti-metastasis property, Ceram. Int. 49 (5) (2023) 7359–7369.
[16] M. Ali Dheyab, A.A. Aziz, M.S. Jameel, Recent advances in inorganic nanomaterials synthesis using sonochemistry: A comprehensive review on iron oxide, gold and iron oxide coated gold nanoparticles, Molecules 26 (9) (2021) 2453.
[17] S.B. Park, S.B. White, C.S. Steadman, T. Pechan, O. Pechanova, H.J. Clemente, R.V. K.G. Thirumalai, S.T. Willard, P.L. Ryan, J.M. Feugang, Silver-coated magnetic nanocomposites induce growth inhibition and protein changes in foodborne bacteria, Sci. Rep. 9 (2019), https://doi.org/10.1038/s41598-019-53080-x.
[18] H. Nosrati, M. Salehiabar, F. Mozafari, J. Charmi, N. Erdoğan, M. Ghaffarlou, F. Abhari, H. Danafar, A. Ramazani, Y. Nuri Ertas, Preparation and evaluation of bismuth sulfide and magnetite-based theranostic nanohybrid as drug carrier and dual MRI/CT contrast agent, Appl. Organomet. Chem. 36 (2022), https://doi.org/10.1002/aoc.6861.
[19] M.A. Shahbazi, L. Faghfouri, M.P.A. Ferreira, P. Figueiredo, H. Maleki, F. Sefat, J. Hirvonen, H.A. Santos, The versatile biomedical applications of bismuth-based nanoparticles and composites: Therapeutic, diagnostic, biosensing, and regenerative properties, Chem. Soc. Rev. 49 (2020) 1253–1321, https://doi.org/10.1039/c9cs00283a.
[20] M. Andrés-Vergés, M. Del Puerto Morales, S. Veintemillas-Verdaguer, F. J. Palomares, C.J. Serna, Core/shell magnetite/bismuth oxide nanocrystals with tunable size, colloidal, and magnetic properties, Chem. Mater. 24 (2012) 319–324, https://doi.org/10.1021/cm202949q.
[21] P.C. Naha, A. Al Zaki, E. Hecht, M. Chorny, P. Chhour, E. Blankemeyer, D.M. Yates, W.R.T. Witschey, H.I. Litt, A. Tsourkas, D.P. Cormode, Dextran coated bismuth-iron oxide nanohybrid contrast agents for computed tomography and magnetic resonance imaging, J. Mater. Chem. B 2 (2014) 8239–8248, https://doi.org/10.1039/c4tb01159g.
[22] S. Badrigilan, B. Shaabani, N. Gharehaghaji, A. Mesbahi, Iron oxide/bismuth oxide nanocomposites coated by graphene quantum dots: "Three-in-one" theranostic agents for simultaneous CT/MR imaging-guided in vitro photothermal therapy, Photodiagn. Photodyn. Ther. 25 (2019) 504–514, https://doi.org/10.1016/j.pdpdt.2018.10.021.
[23] S. Veintemillas-Verdaguer, Y. Luengo, C.J. Serna, M. Andrés-Vergés, M. Varela, M. Calero, A. Lazaro-Carrillo, A. Villanueva, A. Sisniega, P. Montesinos, M. P. Morales, Bismuth labeling for the CT assessment of local administration of magnetic nanoparticles, Nanotechnology 26 (13) (2015) 135101.
[24] A. Rajaee, X. Wensheng, L. Zhao, S. Wang, Y. Liu, Z. Wu, J. Wang, F. Si-Shen, Multifunctional bismuth ferrite nanoparticles as magnetic localized dose enhancement in radiotherapy and imaging, J. Biomed. Nanotechnol. 14 (2018) 1159–1168, https://doi.org/10.1166/jbn.2018.2553.
[25] Y. Xiong, F. Sun, P. Liu, Z. Yang, J. Cao, H. Liu, P. Liu, J. Hu, Z. Xu, S. Yang, A biomimetic one-pot synthesis of versatile Bi2S3/FeS2 theranostic nanohybrids for tumor-targeted photothermal therapy guided by CT/MR dual-modal imaging, Chem. Eng. J. 378 (2019), https://doi.org/10.1016/j.cej.2019.122172.
[26] R. Dolores, S. Raquel, G.L. Adianez, Sonochemical synthesis of iron oxide nanoparticles loaded with folate and cisplatin: Effect of ultrasonic frequency, Ultrason. Sonochem. 23 (2015) 391–398, https://doi.org/10.1016/j.ultsonch.2014.08.005.
[27] C. Gomez, G. Hallot, A. Pastor, S. Laurent, E. Brun, C. Sicard-Roselli, M. Port, Metallic bismuth nanoparticles: Towards a robust, productive and ultrasound assisted synthesis from batch to flow-continuous chemistry, Ultrason. Sonochem. 56 (2019) 167–173, https://doi.org/10.1016/j.ultsonch.2019.04.012.
[28] L. Gao, S. Mei, H. Ma, X. Chen, Ultrasound-assisted green synthesis of gold nanoparticles using citrus peel extract and their enhanced anti-inflammatory activity, Ultrason. Sonochem. 83 (2022) 105940.
[29] M.S. Jameel, A.A. Aziz, M.A. Dheyab, P.M. Khaniabadi, A.A. Kareem, M. Alrosan, A.T. Ali, M.A. Rabeea, B. Mehrdel, Mycosynthesis of ultrasonically-assisted uniform cubic silver nanoparticles by isolated phenols from Agaricus bisporus and its antibacterial activity, Surf. Interfaces 29 (2022) 101774.
[30] B.K. Sodipo, A.A. Aziz, Optimization of sonochemical method of functionalizing Amino-Silane on superparamagnetic iron oxide nanoparticles using Central Composite Design, Ultrason. Sonochem. 64 (2020) 104856.
[31] F.S. Braim, N.N.A. Nik Ab Razak, A.A. Aziz, M.A. Dheyab, L.Q. Ismae, Ultrasound assisted chitosan coated iron oxide nanoparticles: Influence of ultrasonic irradiation on the crystallinity, stability, toxicity and magnetization of the functionalized nanoparticles, Ultrason. Sonochem. 88 (2022) 106072, https://doi.org/10.1016/J.ULTSONCH.2022.106072.
[32] M.A. Dheyab, A.A. Aziz, M.S. Jameel, P.M. Khaniabadi, B. Mehrdel, Mechanisms of effective gold shell on Fe3O4 core nanoparticles formation using sonochemistry method, Ultrason. Sonochem. 64 (2020) 104865.
[33] N.S.M. Yusof, B. Babgi, Y. Alghamdi, M. Aksu, J. Madhavan, M. Ashokkumar, Physical and chemical effects of acoustic cavitation in selected ultrasonic cleaning applications, Ultrason. Sonochem. 29 (2016) 568–576, https://doi.org/10.1016/j.ultsonch.2015.06.013.
[34] R. Mirzajani, S. Karimi, Ultrasonic assisted synthesis of magnetic Ni-Ag bimetallic nanoparticles supported on reduced graphene oxide for sonochemical simultaneous removal of sunset yellow and tartrazine dyes by response surface optimization: Application of derivative spectrophot, Ultrason. Sonochem. 50 (2019) 239–250, https://doi.org/10.1016/j.ultsonch.2018.09.022.
[35] S. Dashamiri, M. Ghaedi, K. Dashtian, M.R. Rahimi, A. Goudarzi, R. Jannesar, Ultrasonic enhancement of the simultaneous removal of quaternary toxic organic dyes by CuO nanoparticles loaded on activated carbon: Central composite design, kinetic and isotherm study, Ultrason. Sonochem. 31 (2016) 546–557, https://doi.org/10.1016/j.ultsonch.2016.02.008.
[36] H. Hassan, S.K. Adam, E. Alias, M.M.R. Meor Mohd Affandi, A.F. Shamsuddin, R. Basir, Central composite design for formulation and optimization of solid lipid nanoparticles to enhance oral bioavailability of acyclovir, Molecules 26 (18) (2021) 5432.
[37] Z. Li, J. Liu, Y. Hu, Z. Li, X. Fan, Y. Sun, F. Besenbacher, C. Chen, M. Yu, Biocompatible PEGylated bismuth nanocrystals: "All-in-one" theranostic agent with triple-modal imaging and efficient in vivo photothermal ablation of tumors, Biomaterials 141 (2017) 284–295, https://doi.org/10.1016/j.biomaterials.2017.06.033.
[38] S.T. Lu, D. Xu, R.F. Liao, J.Z. Luo, Y.H. Liu, Z.H. Qi, C.J. Zhang, N.L. Ye, B. Wu, H. B. Xu, Single-Component Bismuth Nanoparticles as a Theranostic Agent for Multimodal Imaging-Guided Glioma Therapy, Comput. Struct, Biotechnol. J. 17 (2019) 619–627, https://doi.org/10.1016/j.csbj.2019.04.005.
[39] A.Y. Aydar, Utilization of Response Surface Methodology in Optimization of Extraction of Plant Materials. Stat. Approaches With Emphas. Des. Exp. Appl. to Chem. Process., 2018 https://doi.org/10.5772/intechopen.73690.
[40] P. Sahoo, T.K. Barman, ANN modelling of fractal dimension in machining, in: Mechatronics Manuf. Eng., 2012, pp. 159–226, https://doi.org/10.1533/9780857095893.159.
[41] W. Wang, Y. Cheng, G. Tan, Design Optimization of SBS-modified asphalt mixture reinforced with eco-friendly basalt fiber based on response surface methodology, Materials (Basel). 11 (8) (2018) 1311.
[42] T. Mehmood, A. Ahmed, A. Ahmad, M.S. Ahmad, M.A. Sandhu, Optimization of mixed surfactants-based β-carotene nanoemulsions using response surface methodology: An ultrasonic homogenization approach, Food Chem. 253 (2018) 179–184, https://doi.org/10.1016/j.foodchem.2018.01.136.

[43] M. Mahiuddin, B. Ochiai, Green synthesis of crystalline bismuth nanoparticles using lemon juice, RSC Adv. 11 (2021) 26683–26686, https://doi.org/10.1039/d1ra03560f.
[44] J.C. Bulmahn, G. Tikhonowski, A.A. Popov, A. Kuzmin, S.M. Klimentov, A. V. Kabashin, P.N. Prasad, Laser-ablative synthesis of stable aqueous solutions of elemental bismuth nanoparticles for multimodal theranostic applications, Nanomaterials 10 (2020) 1–13, https://doi.org/10.3390/nano10081463.
[45] Y.P. Yew, K. Shameli, M. Miyake, N.B.B. Ahmad Khairudin, S.E.B. Mohamad, H. Hara, M.F.B. Mad Nordin, K.X. Lee, An eco-friendly means of biosynthesis of superparamagnetic magnetite nanoparticles via marine polymer, IEEE Trans. Nanotechnol. 16 (6) (2017) 1047–1052.
[46] K. Murugappan, D.S. Silvester, D. Chaudhary, D.W.M. Arrigan, Electrochemical Characterization of an Oleyl-coated Magnetite Nanoparticle-Modified Electrode, ChemElectroChem 1 (2014) 1211–1218, https://doi.org/10.1002/celc.201402012.
[47] M. Quinten, Optical Properties of Nanoparticle Systems: Mie and beyond, 2011. https://doi.org/10.1002/9783527633135.
[48] Y. Zeng, R. Hu, L. Wang, D. Gu, J. He, S.Y. Wu, H.P. Ho, X. Li, J. Qu, B.Z. Gao, Y. Shao, Recent advances in surface plasmon resonance imaging: Detection speed, sensitivity, and portability, Nanophotonics. 6 (2017) 1017–1030, https://doi.org/10.1515/nanoph-2017-0022.
[49] A. Abbasi Kajani, A.K. Bordbar, Biogenic magnetite nanoparticles: A potent and environmentally benign agent for efficient removal of azo dyes and phenolic contaminants from water, J. Hazard. Mater. 366 (2019) 268–274, https://doi.org/10.1016/j.jhazmat.2018.11.111.
[50] B. Lesiak, N. Rangam, P. Jiricek, I. Gordeev, J. Tóth, L. Kövér, M. Mohai, P. Borowicz, Surface Study of Fe3O4 Nanoparticles Functionalized With Biocompatible Adsorbed Molecules, Front. Chem. 7 (2019), https://doi.org/10.3389/fchem.2019.00642.
[51] Y. Hadadian, H. Masoomi, A. Dinari, C. Ryu, S. Hwang, S. Kim, B.K. Cho, J.Y. Lee, J. Yoon, From low to high saturation magnetization in magnetite nanoparticles: the crucial role of the molar ratios between the chemicals, ACS Omega 7 (2022) 15996–16012, https://doi.org/10.1021/acsomega.2c01136.
[52] P.H. Nam, N.X. Phuc, D.H. Manh, D.K. Tung, V.Q. Nguyen, N.H. Nam, P.K. Son, T. N. Bach, P.T. Phong, Physical characterization and heating efficacy of chitosan-coated cobalt ferrite nanoparticles for hyperthermia application, Phys. E Low-Dimensional Syst. Nanostruct. 134 (2021) 114862.